ЖЭТФ, 2011, том 139, вып. 3, стр. 479–507

STOCHASTIC STATISTICAL THEORY OF NUCLEATION AND EVOLUTION OF NANO-SIZED PRECIPITATES IN ALLOYS WITH AN APPLICATION TO PRECIPITATION OF COPPER IN IRON

K. Yu. Khromov [a,b], ***F. Soisson*** [c], ***A. Yu. Stroev*** [a,b], ***V. G. Vaks*** [a,b*]

[a] *Russian Research Center "Kurchatov Institute"*
123182, Moscow, Russia

[b] *Moscow Institute of Physics and Technology (State University)*
117303, Moscow, Russia

[c] *Service de Recherches de Métallurgie Physique, DMN-SRMP, CEA Saclay*
91191, Gif-sur-Yvette, France

Received June 16, 2010

A consistent and computationally efficient stochastic statistical approach (SSA) is developed to study the kinetics of nucleation and evolution of nano-sized precipitates in alloys. To increase the accuracy of the method, many refinements of the previous simplified versions of this approach have been made. We consider a realistic vacancy-mediated exchange kinetics rather than the simplified direct-atomic-exchange model; use quantitative, cluster statistical methods rather than simple mean-field-type approximations; allow strong concentration and temperature dependences of generalized mobilities in the resulting kinetic equations; consider realistic alloy models based on first-principle calculations, and so on. We also introduce the "maximum thermodynamic gain" principle to determine the key kinetic parameter of the SSA, the characteristic length of local equilibrium in the course of the nucleation process. For several realistic models of iron–copper alloys studied, the results of the SSA-based simulations of precipitation kinetics made in this work agree well with the kinetic Monte Carlo simulation results for all main characteristics of the microstructure. The approach developed is also used to study the kinetics of nucleation and changes in microstructural evolution under variations of temperature or concentration.

1. INTRODUCTION

Studies of microstructural evolution in phase-separating alloys attract interest from both fundamental and applied standpoints. On the fundamental side, elucidation of microscopic mechanisms for the formation and evolution of embryos of new phases arising under first-order phase transitions is one of the principal problems in statistical physics that is still not well understood [1–4]. On the applied side, understanding factors that determine different microstructure characteristics formed under precipitation is important for controlling these characteristics, especially for alloys with nano-sized precipitates, which attract much attention in connection with industrial applications [5–8].

Presently, theoretical studies of the precipitation kinetics typically use either the phase–field method (PFM) [9–14] or Monte Carlo modeling [4, 15–18]. However, using the phase–field methods to describe nucleation and evolution of nano-sized precipitates can be misleading for three reasons at least. First, the "continuous" approximation used in the PFM disregards the discrete lattice effects that should be important at first stages of nucleation when typical precipitate sizes are few lattice constants. Second, at the concentration and temperature values typical for applications, the mean-field-type CALPHAD expressions for thermodynamic potentials standardly used in the PFM studies [9–13] are shown in what follows to strongly distort the position of spinodals, and hence using these expressions can drastically distort the type of microstructural evolution. Third, treatment of fluctuative terms (which are crucial at the nucleation stage) in the "stochastic PFM" versions used in applications until now [9, 10]

*E-mail: vaks@mbslab.kiae.ru

seems to be arbitrary and inconsistent [19, 20], while the correct description of these terms determines all the main characteristics of the microstructure.

Therefore, the only reliable source of theoretical information about nucleation and evolution of nano-sized precipitates is the Monte Carlo modeling, in particular, the kinetic Monte Carlo approach (KMCA) developed in Refs. [4, 15–18]. However, present versions of the KMCA are time-consuming, which may partly explain a relatively small number of applications of this method to specific systems [17, 18]. Moreover, the lattice misfit and elastic strain effects, which are important for many phase-separating alloys, cannot be easily taken into account in the KMCA, while this causes no problems in statistical approaches [21]. Finally, in the KMCA, it is often difficult to follow the dependence of various characteristics of the evolution on thermodynamic and microscopic parameters of an alloy, such as the composition, temperature, different interaction constants, while this is usually much simpler to do using statistical methods based on some analytic relations. Therefore, the development of a consistent statistical theory that takes all achievements of the KMCA into account seems to be very important for a deeper understanding of the phase separation kinetics.

Recently, Stroev et al. [20] (SPV) presented an attempt to develop such a theory using the stochastic statistical approach (SSA) described in Sec. 3.2 below. To illustrate the main ideas of this approach, SPV used only the simplest methods and models, such as the mean field approximation (MFA), continuous approximations, the direct-atomic-exchange (rather than the vacancy exchange) kinetic model, oversimplified interaction models, and so on, while no attempts of a quantitative treatment of realistic alloy models have been made.

The main aim of this paper is to increase the accuracy and the predictive power of the SSA in describing the precipitation kinetics for realistic alloy models up to the level comparable to that of the KMCA. For this, we perform detailed studies of nucleation and evolution of nano-sized precipitates in Fe–Cu alloys using both the KMCA [16, 18] and the SSA. This requires many refinements of simple models used by SPV. We have to consider the realistic vacancy-mediated exchange kinetics rather than the simplified direct-atomic-exchange model; to use the quantitative, cluster statistical methods rather than the simple MFA; to allow strong concentration and temperature dependences of generalized mobilities in the resulting kinetic equations, and so on. All these refinements are made in the present work. We also introduce the "maximum thermodynamic gain" principle to determine the key kinetic parameter of the SSA, the characteristic length of local equilibrium in the course of the nucleation process.

In Sec. 2, we discuss the methodological problems mentioned above: generalizations of our statistical approach to the vacancy-mediated kinetics case; using cluster methods for both thermodynamic and kinetic statistical calculations; elaboration of effective methods for calculations of the effective mobilities that enter the resulting kinetic equations, and so on. We also generalize the previously suggested "equivalence theorem" [22] that allows reducing the vacancy-mediated kinetics to that for some equivalent direct-exchange models. In Sec. 3, we recall the basic ideas of the classical theory of nucleation and present the main equations of the SSA. In Sec. 4, we discuss the models and the methods of simulations used and describe the "maximum thermodynamic gain" principle suggested to estimate the local equilibrium length. In Sec. 5, we discuss the features of microstructural evolution observed in the KMCA and SSA simulations for various alloy states. We also use the SSA to study kinetics of nucleation and the influence of temperature or concentration variations on the evolution of the microstructure. Our main conclusions are summarized in Sec. 6.

2. QUASI-EQUILIBRIUM KINETIC EQUATIONS FOR VACANCY-MEDIATED KINETICS IN SUBSTITUTIONAL ALLOYS

2.1. General equations for mean occupations of lattice sites

In this section, we derive kinetic equations for mean occupations of lattice sites disregarding fluctuations of atomic fluxes that lead to local violations of the second law of thermodynamics. These "quasi-equilibrium kinetic equations" (QKE) differ from the stochastic kinetic equations discussed below (which do take such fluctuations into account) and generalize those used by SPV [20] for simplified direct-atomic-exchange models to more realistic, vacancy-mediated-exchange (VME) models. We also generalize a similar treatment of the VME kinetics by Belashchenko and Vaks [22] (BV) to more realistic VME models used in Refs. [16, 18] and below.

We consider a substitutional alloy with $m+1$ components p' that include atoms of m different species, $p = p_1, p_2, \ldots, p_m$, and vacancies v: $p' = \{p, v\}$. The distributions of atoms over the lattice sites i are described by the different occupation number sets $\{n_i^{p'}\}$, where the operator $n_i^{p'}$ is 1 when the site i is occupied

by a p'-species component and 0 otherwise. For each i, these operators satisfy the identity $\sum_{p'} n_i^{p'} = 1$, and hence only m of them are independent. It is convenient to mark the independent operators with Greek letters ρ or σ: $(n_i^{p'})_{indep} = n_i^\rho$, while the remaining operators denoted as n_i^h are expressed via n_i^ρ:

$$n_i^h = 1 - \sum_\rho n_i^\rho. \tag{1}$$

For dilute alloys, it is convenient to set "h" in (1) to be the host component, e. g., $h =$ Fe for Fe–Cu–v alloys.

In terms of all operators $n_i^{p'}$, the configurational Hamiltonian H' (supposed to be pairwise for simplicity) can be written as

$$H' = \frac{1}{2} \sum_{p'q',ij} V_{ij}^{p'q'} n_i^{p'} n_j^{q'}. \tag{2}$$

After elimination of the operators n_i^h according to (1), Hamiltonian (2) takes the form

$$\begin{aligned} H &= E_0 + \sum_{\rho i} \varphi_\rho n_i^\rho + H_{int}, \\ H_{int} &= \sum_{\rho\sigma, i>j} v_{ij}^{\rho\sigma} n_i^\rho n_j^\sigma \end{aligned} \tag{3}$$

which includes only the independent n_i^ρ, while the constants E_0 and φ_ρ and the "configurational interactions" $v_{ij}^{\rho\sigma}$ are linearly expressed in terms of the couplings $V_{ij}^{p'q'}$ in (2), in particular,

$$v_{ij}^{\rho\sigma} = (V^{\rho\sigma} - V^{\rho h} - V^{h\sigma} + V^{hh})_{ij}. \tag{4}$$

The fundamental master equation for the probability P of finding an occupation number set $\{n_i^\rho\} = \xi$ is [21]:

$$\frac{dP(\xi)}{dt} = \sum_\eta [W(\xi,\eta)P(\eta) - W(\eta,\xi)P(\xi)] \equiv \hat{S}P, \tag{5}$$

where $W(\xi,\eta)$ is the $\eta \to \xi$ transition probability per unit time. Adopting the conventional "transition state" model for the probabilities W [4, 15, 16, 18], we can express the transfer matrix $\hat{S}$ in (5) in terms of the probability of an elementary inter-site exchange ("jump") $pi \rightleftharpoons vj$ between neighboring sites i and j:

$$W_{ij}^{pv} = n_i^p n_j^v \omega_{pv} \exp[-\beta(\hat{E}_{pi,vj}^{SP} - \hat{E}_{pi,vj}^{in})], \tag{6}$$

where ω_{pv} is the attempt frequency, $\beta = 1/T$ is the reciprocal temperature, $\hat{E}_{pi,vj}^{SP}$ is the saddle-point energy, and $\hat{E}_{pi,vj}^{in}$ is the initial (before the jump) configurational energy of the jumping atom p and the vacancy. The saddle-point energy $\hat{E}_{pi,vj}^{SP}$, generally, depends on the atomic configuration near the bond ij (which is neglected in simplified kinetic models [4, 15, 22]). We describe this dependence by the model used in Refs. [16] and [18], assuming the saddle-point energy to depend only on occupations of lattice sites l nearest to the center of the ij bond (these sites are denoted by l_{nn}^{ij}):

$$\hat{E}_{pi,vj}^{SP} = \sum_{q, l=l_{nn}^{ij}} \varepsilon_q^p n_l^q = E_h^p - \hat{\Delta}_{ij}^p. \tag{7}$$

Here, E_h^p is the saddle-point energy for the pure host metal, and the operator $\hat{\Delta}_{ij}^p$ describes changes in this energy due to a possible presence of minority atoms near the bond:

$$E_h^p = z_{nn}^b \varepsilon_h^p, \quad \hat{\Delta}_{ij}^p = \sum_{\rho,\, l=l_{nn}^{ij}} \Delta_\rho^p n_l^\rho, \tag{8}$$

where z_{nn}^b is the total number of nearest lattice sites l for each bond (which is $z_{nn}^b = 6$ for a BCC lattice) and $\Delta_\rho^p = (\varepsilon_h^p - \varepsilon_\rho^p)$.

As discussed in detail in [21], under the usual conditions of phase transitions corresponding to the absence of external fluxes of particles or energy (that is, when the alloy is not an "open" but a "closed" statistical system), the distribution function $P(\xi) = P\{n_i^\rho\}$ in (5) can be written as

$$P\{n_i^\rho\} = \exp\left[\beta\left(\Omega + \sum_{\rho i} \lambda_i^\rho n_i^\rho - H_{int}\right)\right]. \tag{9}$$

The parameters λ_i^ρ (which are both time- and space-dependent in general) can be called "site chemical potentials" for ρ-species atoms; H_{int} is the same as in (3); and the generalized grand canonical potential Ω is determined by normalization. The analogous equation (10) of BV [22] (who treated both closed and open systems) differs from (9) by replacing the interaction Hamiltonian with a more general "quasi-interaction" operator Q. For the closed systems discussed in this work, $Q = H_{int}$, and this relation greatly simplifies the kinetic equations discussed below compared to those of BV.

Multiplying Eq. (5) by operators n_i^ρ and summing over all configurational states, i. e., over all number sets $\{n_i^\rho\}$, we obtain the set of equations for mean occupations of sites ("local concentrations") $c_i^\rho = \langle n_i^\rho \rangle$:

$$\frac{dc_i^\rho}{dt} = \langle n_i^\rho \hat{S} \rangle, \tag{10}$$

where $\langle (\dots) \rangle = \mathrm{Tr}\{(\dots)P\}$ denotes averaging over the distribution P, for example,

$$c_i^\rho = \langle n_i^\rho \rangle = \sum_{\{n_j^\sigma\}} c_i^\rho P\{n_j^\sigma\}. \tag{11}$$

After a number of manipulations described by BV, Eqs. (10) can be transformed into the QKE for mean occupations c_i^ρ. These equations are similar to Eqs. (19) and (42) of BV [22] but include generalizations and simplifications mentioned above:

$$\frac{dc_i^\alpha}{dt} = \sum_{j_{nn}(i)} \gamma_{\alpha v} b_{ij}^\alpha (\xi_i^v \eta_j^\alpha - \xi_j^v \eta_i^\alpha), \tag{12}$$

$$\frac{dc_i^v}{dt} = \sum_{j_{nn}(i)} \left[\xi_j^v \left(\gamma_{hv} b_{ij}^h + \sum_\beta \gamma_{\beta v} b_{ij}^\beta \eta_i^\beta \right) - \right. \\ \left. - \{i \to j\} \right]. \tag{13}$$

Here and hereafter, Greek indices $\alpha, \beta \ldots$ correspond to the minority atoms; the symbol "v" is used for vacancies; the index nn means "nearest neighbors", and "$j_{nn}(i)$" means summation over sites j that are nearest neighbors of the site i. The term γ_{pv} in (13) (where p is α or h, i. e., a minority or host atom) is the effective exchange rate $p \rightleftharpoons v$ for a pure host metal. This term can be written in a form similar to Eq. (6):

$$\gamma_{pv} = \omega_{pv} \exp(-\beta E_{ac}^{pv}), \tag{14}$$

where ω_{pv} is the same as in (6), while E_{ac}^{pv} is the effective activation energy expressed in terms of the saddle-point energies E_h^p in (8) and couplings $V_{ij}^{p'q'}$ in (2) as

$$E_{ac}^{pv} = E_h^p - \sum_j (V_{ij}^{ph} + V_{ij}^{vh}) + V_{nn}^{hh}. \tag{15}$$

We note that for minority atoms $p = \alpha$, expressions (15) differ from analogous activation energies $E_{ac,MC}^{pv}$ used in the KMCA and given by Eq. (2.5) in Ref. [16]:

$$E_{ac}^{\alpha v} = E_{ac,MC}^{\alpha v} + v_{nn}^{\alpha v}; \quad E_{ac}^{hv} = E_{ac,MC}^{hv}. \tag{16}$$

The difference arises because in the statistically averaged Eqs. (12) and (13), probability (6) is averaged over distribution (9), and for the inter-site exchange $\alpha i \rightleftharpoons vj$, it leads to an extra Gibbs factor $\exp(-\beta v_{ij}^{\alpha v})$ in the averaged probability.

The quantities b_{ij}^p in (13) (to be called "correlators" for brevity) are certain averages of site occupations that describe the effect of minority atoms in a vicinity of the bond ij on the $pi \rightleftharpoons vj$ jump probability:

$$b_{ij}^p = \left\langle n_i^h n_j^h \exp\left[\sum_{\alpha l} \beta (u_{il}^\alpha + u_{jl}^\alpha) n_l^\alpha + \right. \right. \\ \left. \left. + \sum_{\alpha,\, l = l_{nn}^{ij}} \beta \Delta_\alpha^p n_l^\alpha \right] \right\rangle, \tag{17}$$

where Δ_α^p is the same as in (8), while the quantities u_{il}^α (to be called "kinetic interactions" because they affect only the effective jump probabilities but not thermodynamic properties) are related to the couplings $V_{ij}^{p'q'}$ in (2) as

$$u_{il}^\alpha = V_{il}^{\alpha h} - V_{il}^{hh}. \tag{18}$$

Finally, the quantities ξ_i^v and η_i^α in (13) and (12) can be called "site thermodynamic activities" for vacancies and α-species atoms because they are related to the site chemical potentials λ_i^ρ in (9) as

$$\xi_i^v = \exp(\beta \lambda_i^v), \quad \eta_i^\alpha = \exp(\beta \lambda_i^\alpha), \tag{19}$$

that is, similarly to the relations between conventional thermodynamic activities and chemical potentials.

2.2. Calculations of the site chemical potentials λ_i^ρ and correlators b_{ij}^p

To solve QKE (13), we need explicit expressions for the site chemical potentials $\lambda_i^\rho = \lambda_i^\rho(c_j)$ determined by Eqs. (11), and for correlators $b_{ij}^p = b_{ij}^p(c_k)$ determined by Eqs. (17). To find these expressions, we should use some approximate method of statistical physics, such as the MFA or cluster methods [21]. As discussed in detail in [23, 24] and below, at the realistic values of the couplings $v_{ij}^{\alpha\beta}$ that significantly exceed the temperature T (which is typical, in particular, for the iron–copper alloys under consideration), using the MFA leads to great errors in calculations of thermodynamic potentials, which excludes any realistic description. At the same time, the pair cluster approximation (PCA) usually combines the simplicity of calculations with a rather high accuracy, particularly at low c and T under consideration (see, e. g., [23–25]). For the site chemical potentials λ_i^ρ, we therefore use their PCA expressions, which for a binary alloy ABv with minority atoms A, host atoms B, and a realistically small concentration of vacancies $c_i^v \ll 1$ are given by Eqs. (39) of BV:

$$\lambda_i = T \left[\ln\left(\frac{c_i}{c_i^h}\right) + \sum_{j \neq i} \ln(1 - g_{ij} c_j) \right], \tag{20}$$

$$\lambda_i^v = T \left[\ln\left(\frac{c_i^v}{c_i^h}\right) - \sum_{j \neq i} \ln(1 + g_{ij}^v c_j) \right]. \tag{21}$$

Here, $\lambda_i = \lambda_i^A$, $c_i = c_i^A$, $c_i^h = (1 - c_i - c_i^v) \approx (1 - c_i)$, and the function g_{ij} or g_{ij}^v is expressed in terms of the Mayer function $f_{ij} = [\exp(-\beta v_{ij}) - 1]$ or $f_{ij}^v = [\exp(-\beta v_{ij}^{vA}) - 1]$ for the potential $v_{ij} \equiv v_{ij}^{AA}$ or v_{ij}^{vA} defined in (4),

$$\begin{aligned} v_{ij} &= V_{ij}^{AA} - 2V_{ij}^{AB} + V_{ij}^{BB}, \\ v_{ij}^{vA} &= V_{ij}^{vA} - V_{ij}^{Bv} - V_{ij}^{AB} + V_{ij}^{BB}, \end{aligned} \tag{22}$$

as follows:

$$\begin{aligned} g_{ij} &= 2f_{ij}/[R_{ij} + 1 + f_{ij}(c_i + c_j)], \\ g_{ij}^v &= 2f_{ij}^v/[R_{ij} + 1 + f_{ij}(c_i - c_j)], \\ R_{ij} &= \left\{[1+(c_i+c_j)f_{ij}]^2 - 4c_ic_jf_{ij}(f_{ij}+1)\right\}^{1/2}. \end{aligned} \tag{23}$$

We also present the PCA expression for the free energy F of a binary alloy [21], to be used in Sec. 4.2 below in discussing the thermodynamics of precipitation:

$$F = \sum_i T \ln c_i^h - T\frac{1}{2}\sum_{ij} \ln(1 - g_{ij}c_ic_j) + \\ + \sum_i \lambda_i c_i, \tag{24}$$

where g_{ij} is the same as in (23). If the temperature T much exceeds the couplings v_{ij}, $T \gg v_{ij}$, PCA expressions (20) and (24) transform into the MFA ones [21]. However, as mentioned, the opposite inequality $T \ll v_{ij}$ typically holds in situations of practical interest, and using the MFA is misleading.

We now discuss the calculation of the correlators b_{ij}^p in (17). For simplicity, we first consider the case of configuration-independent saddle-point energies when the differences Δ_α^p in Eqs. (8) and (17) vanish and the correlators $b_{ij}^p = b_{ij}$ are independent of the kind of a jumping atom p. Using the identities

$$\begin{aligned} &(n_l^\alpha)^2 = n_l^\alpha, \quad n_l^\alpha n_l^\beta = n_l^\alpha \delta_{\alpha\beta}, \quad n_l^\alpha n_l^h = 0, \\ &\exp(xn_l^\alpha) = 1 + n_l^\alpha f(x), \quad f(x) = (e^x - 1), \end{aligned} \tag{25}$$

we can rewrite Eq. (17) as

$$\begin{aligned} b_{ij} &= \left\langle n_i^h n_j^h \prod_{l=1}^{k_t} \left(1 + \sum_\alpha f_l^\alpha n_l^\alpha\right)\right\rangle = \\ &= \sum_{k=0}^{k_t} \sum_{l_1\neq\ldots l_k} \sum_{\alpha_1\ldots\alpha_k} \left\langle n_i^h n_j^h n_{l_1}^{\alpha_1} \ldots n_{l_k}^{\alpha_k}\right\rangle \times \\ &\qquad \times f_{l_1}^{\alpha_1} \ldots f_{l_k}^{\alpha_k}, \end{aligned} \tag{26}$$

where we set

$$f_l^\alpha = f(\beta u_{il}^\alpha + \beta u_{jl}^\alpha) \tag{27}$$

with $f(x)$ from (25), and k_t in (26) is the total number of sites with nonzero values of potentials $u_{il}^\alpha + u_{jl}^\alpha$. For example, for the nearest-neighbor or next-to-nearest-neighbor interaction models in a BCC lattice, we have $k_t = 14$ or $k_t = 20$.

To find averages over distribution (9) in (26), we should again use some approximate method of calculations, such as the MFA, PCA, or higher-order cluster approximations [21, 25]. However, for most of the systems of practical interest, in particular, for the iron–copper alloys discussed below, we can apparently use the simple MFA in (26), replacing each operator n_l^α with its mean $c_l^\alpha = \langle n_l^\alpha\rangle$. This seems to be justified because the functions f_l^α in Eqs. (26) and (27) for such systems are typically rather large (for example, $f(\beta u_1) \gtrsim 5$ for the systems described in Table 3 below). Therefore, the main contributions to sum (26) come from averages of products of many different operators n_l^α corresponding to well-separated and weakly correlated sites l. In particular, for the BCC lattice, these products (even for the nearest-neighbor interaction model) include terms with the neighbors from the first to the tenth, most often third and fourth. Correlations of occupations for so distant lattice sites should typically be small, and hence using the MFA that neglects such correlations should be adequate.

In the MFA, Eq. (26) takes the form

$$b_{ij} = c_i^h c_j^h \sum_{k=0}^{k_t} \sum_{l_1\neq\ldots l_m\neq i,j} \sum_{\alpha_1\ldots\alpha_k} c_{l_1}^{\alpha_1} \ldots c_{l_k}^{\alpha_k} \times \\ \times f_{l_1}^{\alpha_1} \ldots f_{l_k}^{\alpha_k}. \tag{28}$$

To further simplify this expression, we can take into account that spatial variations of the local concentration c_l^α arising in the course of alloy decomposition are typically rather smooth, especially at the nucleation stage (for which an adequate description of kinetic coefficients that include the correlators b_{ij} is most important), see, e. g., Figs. 20–22 below. Hence, the c_l^α values for sites l adjacent to the ij bond that enter Eq. (28) are usually close to both the c_i^α and c_j^α, as well as to their mean

$$\bar{c}_{ij}^{\,\alpha} = (c_i^\alpha + c_j^\alpha)/2. \tag{29}$$

Therefore, to avoid unnecessary computational complications, we can approximate each c_l^α in Eq. (28) by the mean (29). This allows writing the correlator b_{ij} in (28) in a simple analytic form,

$$b_{ij} = c_i^h c_j^h \prod_{l\neq i,j}^{k_t} \left(1 + \sum_\alpha \bar{c}_{ij}^{\,\alpha} f_l^\alpha\right). \tag{30}$$

For example, for a binary alloy ABv in the BCC lattice described by the second-neighbor interaction model with two kinetic interaction constants u_1 and u_2, we obtain

$$b_{ij} = c_i^h c_j^h \,[1 + \bar{c}_{ij} f(\beta u_1 + \beta u_2)]^6 \times \\ \times\, [1 + \bar{c}_{ij} f(\beta u_1)]^8 [1 + \bar{c}_{ij} f(\beta u_2)]^6, \quad (31)$$

where the superscript $\alpha = A$ in $c_{ij}^{\,\alpha}$ and u_n^α is omitted for brevity.

When the differences Δ_α^p in Eqs. (8) and (17) are nonzero, the correlator b_{ij}^p in Eq. (17) can be calculated in the same way as b_{ij} in Eqs. (26)–(31). The difference arises only for sites $l = l_{nn}^{ij}$ adjacent to the ij bond, for which the factors f_l^α defined by Eq. (27) are replaced by analogous factors $f_\Delta^{\alpha p}$ defined as

$$f_\Delta^{\alpha p} = f(\beta u_{il}^\alpha + \beta u_{j\,l}^\alpha + \beta \Delta_\alpha^p). \quad (32)$$

In particular, for the BCC binary alloy ABv with the next-to-nearest-neighbor interaction, instead of (31), we obtain

$$b_{ij}^p = c_i^h c_j^h \,[1 + \bar{c}_{ij} f_\Delta^{Ap}]^6 \times \\ \times\, [1 + \bar{c}_{ij} f(\beta u_1)]^8 [1 + \bar{c}_{ij} f(\beta u_2)]^6, \quad (33)$$

where $f_\Delta^{Ap} = f[\beta(u_1 + u_2 + \Delta^p)]$ and $\Delta^p = \varepsilon_h^p - \varepsilon_A^p$.

2.3. Equivalence of precipitation kinetics for vacancy-mediated exchange models to that for certain direct-exchange models

In this section, we show that the VME kinetics described by Eqs. (12) and (13) can usually be described in terms of certain equivalent direct-atomic-exchange (DAE) models. This generalizes the analogous "equivalence theorem" derived by BV.

We first note that the vacancy activity $\xi_i^v = \exp(\beta\lambda_i^v)$ in Eqs. (12) and (13) is proportional to the vacancy concentration c_i^v. This is illustrated by Eqs. (21) and is actually a general relation of thermodynamics of dilute solutions. Therefore, time derivatives of mean occupations are proportional to the local vacancy concentration c_i^v or c_j^v, which is natural for the vacancy-mediated kinetics. Because c_i^v is very small in real alloys, this implies that the relaxation times of atomic distribution $\{c_i^\alpha\}$ are by a factor $1/c_i^v$ greater than the time of the relaxation of vacancies at the given $\{c_i^\alpha\}$ to their "quasi-equilibrium" distribution $c_i^v\{c_i^\alpha\}$, for which the right-hand side of Eq. (13) vanishes. Therefore, discarding small corrections of the relative order $c_i^v \ll 1$, we can rewrite Eq. (13) as

$$0 = \sum_{j_{nn}(i)} \left[\xi_j^v \left(\gamma_{hv} b_{ij}^h + \sum_\alpha \gamma_{\alpha v} b_{ij}^\alpha \eta_i^\alpha \right) - \right. \\ \left. - \{i \to j\} \right], \quad (34)$$

which can be called "the adiabaticity equation" for the vacancy activity ξ_i^v. Solving this linear equation, we can, in principle, express ξ_i^v in terms of c_j^α. Substituting these $\xi_i^v(c_j^\alpha)$ in Eq. (12) then yields the QKE for some equivalent DAE model.

To illustrate this approach, we first consider the VME models with configuration-independent saddle-point energies. For such models, the parameters Δ_ρ^p in (8) are zero, the correlators $b_{ij}^p = b_{ij}$ are independent of the species p of a jumping atom, and adiabaticity equation (34) takes the simple form

$$\sum_{j_{nn}(i)} b_{ij}\, \xi_i^v \xi_j^v \left[\left(\gamma_{hv} + \sum_\alpha \gamma_{\alpha v} \eta_i^\alpha \right) / \xi_i^v - \right. \\ \left. - \{i \to j\} \right] = 0. \quad (35)$$

If we let $1/\nu_i$ denote the first term in the square brackets (35), then the difference in these brackets takes the form $\nu_i^{-1} - \nu_j^{-1}$. Hence, a solution of Eqs. (35) is given by ν_i being a constant independent of the site number i (although possibly depending on time as well as on temperature and other external parameters):

$$\nu_i = \xi_i^v \Big/ \left(\gamma_{hv} + \sum_\alpha \gamma_{\alpha v} \eta_i^\alpha \right) = \nu(t). \quad (36)$$

Relation (36) determines the above "quasi-equilibrium" vacancy distribution $c_i^v\{c_i^\alpha\}$, which adiabatically fast follows the atomic distribution $\{c_i^\alpha\}$. Substituting it in Eq. (12), we obtain an explicit kinetic equation for atomic distributions $\{c_i^\alpha\}$ for which the evolution of the vacancy distribution is characterized by a single parameter $\nu(t)$ being a "spatially self-averaged" quantity:

$$\frac{dc_i^\alpha}{dt} = \sum_{j_{nn}(i)} b_{ij} \nu(t) \Big[\gamma_{\alpha v} \gamma_{hv} \Big(\eta_j^\alpha - \eta_i^\alpha \Big) + \\ + \sum_\beta \gamma_{\alpha v} \gamma_{\beta v} \Big(\eta_j^\alpha \eta_i^\beta - \eta_i^\alpha \eta_j^\beta \Big) \Big]. \quad (37)$$

The last term in this equation (erroneously missed in the analogous Eq. (46) of BV) is present only for many-component alloys with two or more species of minority atoms. Equations (37) can also be rewritten in the form used for DAE models [21]:

$$\frac{dc_i^\alpha}{dt} = \sum_{j_{nn}(i)} M_{ij}^{\alpha h} 2\,\mathrm{sh}\left[\frac{\beta}{2}(\lambda_j^\alpha - \lambda_i^\alpha)\right] + \\ + \sum_{j_{nn}(i),\beta} M_{ij}^{\alpha\beta} 2\,\mathrm{sh}\left[\frac{\beta}{2}(\lambda_j^\alpha + \lambda_i^\beta - \lambda_i^\alpha - \lambda_j^\beta)\right], \quad (38)$$

where the generalized mobilities M_{ij}^{pq}, which describe inter-site exchanges $\alpha \rightleftharpoons h$ and $\alpha \rightleftharpoons \beta$, are given by

$$M_{ij}^{\alpha h} = \gamma_{\alpha v}\gamma_{hv}\nu(t)\, b_{ij} \exp\left[\frac{\beta}{2}(\lambda_i^\alpha + \lambda_j^\alpha)\right], \quad (39)$$

$$M_{ij}^{\alpha\beta} = \gamma_{\alpha v}\gamma_{\beta v}\nu(t)\, b_{ij} \times \\ \times \exp\left[\frac{\beta}{2}(\lambda_i^\alpha + \lambda_j^\alpha + \lambda_i^\beta + \lambda_j^\beta)\right]. \quad (40)$$

Comparing these expressions with Eq. (32) of BV for the mobilities M_{ij}^{pq} in an alloy with the nearest-neighbor direct-exchange rates $\gamma_{ij}^{pq} = \gamma_{pq}$, we see that Eqs. (39) and (40) correspond to a DAE model with the effective direct exchange rates

$$\gamma_{\alpha h}^{eff} = \gamma_{\alpha v}\gamma_{hv}\,\nu(t), \quad \gamma_{\alpha\beta}^{eff} = \gamma_{\alpha v}\gamma_{\beta v}\,\nu(t). \quad (41)$$

We note that the effective DAE rates in (41) are by a factor c_v smaller than the vacancy exchange rates γ_{pv}.

We next consider more realistic VME models with configuration-dependent saddle-point energies in the case where the correlators b_{ij}^p in (17) are different for different p. For such models, the basic adiabaticity equation (34) for vacancy activities ξ_i^v cannot be solved analytically in general, and hence either numerical or some approximate analytic methods should be used. We discuss two such approximate methods below. For a binary alloy, we can rewrite Eq. (34) as

$$\sum_{j_{nn}(i)} b_{ij}^h\, \xi_i^v \xi_j^v \gamma_{hv} \left(\frac{1+\eta_i r_{ij}}{\xi_i^v} - \frac{1+\eta_j r_{ij}}{\xi_j^v}\right) = 0, \quad (42)$$

where $\eta_i = \eta_i^\alpha = \exp(\beta\lambda_i)$ and $r_{ij} = \gamma_{\alpha v} b_{ij}^\alpha / \gamma_{hv} b_{ij}^h$. Equation (42) can be solved approximately if the products $r_{ij}\eta_i$ obey either of the two inequalities:

$$\eta_i r_{ij} = \exp(\beta\lambda_i)\gamma_{\alpha v} b_{ij}^\alpha / \gamma_{hv} b_{ij}^h \ll 1, \quad (43a)$$

$$\eta_i r_{ij} = \exp(\beta\lambda_i)\gamma_{\alpha v} b_{ij}^\alpha / \gamma_{hv} b_{ij}^h \gg 1. \quad (43b)$$

In case (43a), the second terms in round brackets in (42) are just small corrections to the first ones. They can be neglected in the zeroth approximation, and hence the zeroth-order solution of Eq. (42) is

$$\xi_i^v(i) = \nu(t)\gamma_{hv}, \quad (44)$$

where the constant factor γ_{hv} is introduced such that the function $\nu(t)$ is analogous to that in (36). Substituting (44) in (12), we again obtain Eqs. (37) or (38) for a binary alloy:

$$dc_i/dt = \sum_{j_{nn}(i)} M_{ij}\, 2\,\mathrm{sh}\left[\frac{\beta}{2}(\lambda_j - \lambda_i)\right]. \quad (45)$$

The superscript αh at the effective mobility $M_{ij}^{\alpha h} = M_{ij}$ is omitted for brevity, and the expression for this mobility is similar to that in Eq. (39):

$$M_{ij}(a) = \gamma_{\alpha h}^{eff}\, b_{ij}^\alpha \exp\left[\frac{\beta}{2}(\lambda_i + \lambda_j)\right], \quad (46)$$

with $\gamma_{\alpha h}^{eff}$ being the same as in (41).

In case (43b), we can rewrite Eq. (42) as

$$\sum_{j_{nn}(i)} b_{ij}^\alpha\, \xi_i^v \xi_j^v \gamma_{\alpha v} \left(\frac{\eta_i + r_{ij}^{-1}}{\xi_i^v} - \frac{\eta_j + r_{ij}^{-1}}{\xi_j^v}\right) = 0, \quad (47)$$

where the second terms in the brackets are again small corrections to the first ones. Therefore, the zeroth-order solution of this equation can be written as $\xi_i^{v(0)} = \nu(t)\gamma_{\alpha v}\eta_i$, while corrections are proportional to r_{ij}^{-1}. However, taking these corrections into account is necessary to obtain a nonzero right-hand side of Eq. (12). In finding these small corrections, we can employ the approximation of a "smooth distribution of local concentrations" used to proceed from Eq. (28) to (30); that is, we can assume the r_{ij} values for all bonds ij of a given site i to be close to one another:

$$r_{ij} \approx r_{ii} \approx r_{jj}. \quad (48)$$

Then the solution of Eq. (47) with the first-order corrections is given by

$$\xi_i^v = \nu(t)\gamma_{\alpha v}\left(\eta_i + r_{ij}^{-1}\right). \quad (49)$$

Substituting (49) in (12), we again obtain Eq. (45), but with the correlator b_{ij}^α in the effective mobility (46) replaced by b_{ij}^h:

$$M_{ij}(b) = \gamma_{\alpha h}^{eff}\, b_{ij}^h \exp\left[\frac{\beta}{2}(\lambda_i + \lambda_j)\right]. \quad (50)$$

Physically, the possibility to reduce the vacancy-mediated kinetics to the equivalent direct exchange kinetics is connected with the above-mentioned fact that in the course of evolution of an alloy, the distribution of vacancies follows that of the main components adiabatically fast. Therefore, it can be assumed

that this equivalence not only holds for simplified models (36) or (43) but also is a general feature of the vacancy-mediated kinetics, while for more general models, the correlators b_{ij}, b_{ij}^{α} or b_{ij}^{h} in Eqs. (39), (40), (46) or (50) are probably replaced by some more complex expressions with similar properties.

The function $\nu(t)$ in Eq. (41) determines the rescaling of time between the initial VME model and the equivalent DAE model in (45). Temporal evolution of this DAE model is actually described by the "reduced time" t_r related to the real time t by the differential or integral relations

$$dt_r = \gamma_{\alpha h}^{eff}\, dt = \gamma_{\alpha v}\gamma_{hv}\nu(t)\, dt, \qquad t_r = \int\limits_0^t \gamma_{\alpha h}^{eff}(t')\, dt', \tag{51}$$

$$t = \int\limits_0^{t_r} \tau_{\alpha h}^{eff}(t'_r)\, dt'_r, \tag{52}$$

where $\tau_{\alpha h}^{eff} = (\gamma_{\alpha h}^{eff})^{-1}$ has the meaning of the mean time of an atomic exchange $\alpha \leftrightharpoons h$, while t_r has the meaning of an effective number of such atomic exchanges. This natural physical variable is used below in describing the SSA simulation results.

To find the "rescaling function" $\nu(t)$ in Eqs. (36)–(52), we should, generally, compare the results of simulation of precipitation based on DAE model (45) to those based on the initial VME model. BV made such a comparison for some simplified model of spinodal decomposition, and we estimate $\nu(t)$ below for several realistic models of FeCu alloys using comparison to the KMCA results. We note that the problem of time rescaling between the real physical time and the time units used in the chosen simulation method (e. g., the number of Monte Carlo steps in the KMCA) persists in all simulations of VME kinetics (see Sec. 4.3 below), and it strongly depends, in particular, on the boundary conditions for vacancies adopted in simulations. For example, BV used the "vacancy conservation" model, while in simulations in [16, 18] and below, a possible creation of vacancies at various lattice defects (grain boundaries, dislocations, and so on) is taken into account. Therefore, the form of the function $\nu(t)$ also depends on the kinetic model used for vacancies.

The results presented in Fig. 10 below show that temporal variations of $\nu(t)$ can be rather sharp. These variations arise due to qualitative changes in the distribution of vacancies with respect to minority atoms in the course of the evolution, which are related to the phenomenon of "vacancy trapping" at interfaces of precipitates discussed in detail by BV and by Soisson and Fu [18] (SF). The resulting excess of vacancies near growing or shrinking interfaces leads to an acceleration of the effective exchange rates γ^{eff} with respect to the incubation stage when the precipitates are absent. It results in an increase in $\gamma^{eff}(t)$ after the beginning of nucleation; when the vacancy trapping effect is strong, this increase can be very large, which is illustrated by Fig. 10 below. At the same time, after the nucleation stage is over, the degree of this trapping does not change significantly. Therefore, the function $\nu(t)$ can be expected to be approximately constant before and after the nucleation and to monotonically increase with t in the course of nucleation, as illustrated by Fig. 3 of BV for $\nu(t)$ in their simplified model.

3. MAIN EQUATIONS OF THE STOCHASTIC STATISTICAL APPROACH

3.1. Basic ideas of the classical theory of nucleation

Before describing the SSA, it is convenient to recall the main ideas of the classical nucleation theory (CNT) [1–4]. The CNT treats embryos of a new phase within the original metastable phase as sufficiently large objects arising due to thermodynamic fluctuations. In the simplest version of the CNT, the embryo is regarded as a homogeneous droplet characterized by its radius R, the interface energy σ, and the free energy gain (with respect to the original metastable phase) per unit volume Δf. The excess free energy needed to form this embryo is

$$F(R) = 4\pi R^2\sigma - (4\,\pi R^3/3)\,\Delta f\,. \tag{53}$$

One of the basic CNT notions is the critical embryo that can grow with no further loss of the free energy and hence with no fluctuations. For the model in (53), this corresponds to the maximum of $F(R)$ with respect to R, and therefore the critical radius R_c and the nucleation barrier $F_c = F(R_c)$ are

$$R_c = 2\sigma/\Delta f, \quad F_c = 16\pi\sigma^3/3\Delta f^2, \tag{54}$$

while the probability of the critical fluctuation needed to create this embryo is estimated according to the thermodynamic fluctuation theory [1] as

$$W_c \sim \exp(-F_c/T) \sim \exp(-\text{const}\ \sigma^3/T\Delta f^2). \tag{55}$$

A Ginzburg–Landau-type free energy functional was used in [26] to allow for the diffuse character of

the interface of the critical embryo, but this approach is valid only at high $T \sim T_c$ and for large embryos when the discrete lattice effects can be neglected. A quantitative approach to the calculation of thermodynamics of critical embryos developed in [27, 28] takes the discrete lattice effects into account and uses the PCA rather than the simple MFA. Some results of this approach are used below in Table 2 and Fig. 2.

For supercritical embryos with $R > R_c$, the CNT suggests fluctuation effects to be insignificant. Therefore, after completion of nucleation, the main type of microstructural evolution is the growth of embryos due to the diffusional flux of minority atoms from the matrix. Later on, when larger precipitates grow at the expense of smaller ones, the evaporation–condensation (or Lifshits–Slyozov–Wagner, LSW) mechanism becomes dominant [2]. Therefore, according to the CNT, decomposition of metastable solid solutions should include four well-defined stages [4]: (i) the incubation stage that precedes the formation of first critical and supercritical embryos; (ii) the nucleation stage during which the supercritical precipitate density d_s reaches its maximum value; (iii) the growth stage when the density $d_s(t)$ remains approximately constant but sizes of precipitates grow, and (iv) the coarsening stage when the density $d_s(t)$ decreases due to the LSW evaporation–condensation mechanism.

These CNT ideas were confirmed by KMC simulations of Soisson and Martin [4] (SM) for some simple alloy model for which critical sizes and nucleation barriers (estimated in Table 2 below) are rather large (see, e. g., Fig. 1 in [4]). But in this work, we mainly consider more realistic models of FeCu alloys described in Sec. 4, for which the nucleation barriers and critical sizes are not large. Fluctuation effects in such alloys are shown below to be strong and important not only for the nucleation but also for the growth stage.

3.2. Stochastic kinetic equation and filtration of noise

Quasi-equilibrium kinetic equations (10), (38), and (45) determine evolution of mean occupations of sites due to the average atomic fluxes across each bond. But these averaged equations can describe only those kinetic processes in which the total free energy F_{tot} decreases [22, 29], whereas nucleation process should be accompanied by a fluctuative increase in F_{tot}, needed to overcome nucleation barriers. Therefore, to describe this process, we should consider fluctuations of atomic fluxes. The stochastic statistical approach for taking such fluctuations into account was suggested by SPV [20]. In this section, we present the main equations of this approach; their refinements are described below in Sec. 4.

We consider a binary alloy for which the QKE has form (45). In the SSA, this QKE is replaced by a stochastic kinetic equation (SKE) that can be conveniently written in a finite-difference form (for a short time interval δt) given by Eq. (19) of SPV [20]:

$$\delta c_i \equiv c_i(t+\delta t) - c_i(t) = \delta c_i^d + \sum_{j_{nn}(i)} \delta n_{ij}^f. \qquad (56)$$

Here, c_i is the occupation of site i averaged over some locally equilibrated vicinity of this site, and the "diffusion" term δc_i^d corresponds to the average atomic transfer to site i described by the right-hand side of QKE (45):

$$\delta c_i^d\{c_k\} = \sum_{j_{nn}(i)} M_{ij} 2\,\mathrm{sh}\left[\frac{\beta}{2}(\lambda_j - \lambda_i)\right] \delta t. \qquad (57)$$

The last term δn_{ij}^f in SKE (56) is the fluctuative atomic transfer through the ij bond, which is described by the Langevin-noise-type method: each δn_{ij}^f is treated as a random quantity with the Gaussian probability distribution

$$W(\delta n_{ij}^f) = A_{ij} \exp[(-\delta n_{ij}^f)^2/2D_{ij}], \qquad (58)$$

where A_{ij} is the normalization constant and the dispersion D_{ij} is the same as that for the actual fluctuative transfer δn_{ij}^f. This dispersion is related to the mobility M_{ij} and the time interval δt in Eq. (57) by the "fluctuation–dissipation" type relation (18) of SPV:

$$D_{ij} = \langle(\delta n_{ij}^f)^2\rangle = 2M_{ij}\,\delta t. \qquad (59)$$

For the nonuniform statistical systems under consideration, unlike in standard applications of the Langevin-noise method to mechanical systems, Eqs. (56)–(59) should be supplemented by the "filtration of noise" procedure that eliminates the short-wave contributions to fluctuations δn_{ij}^f. As discussed in detail by SPV, these contributions to Eq. (45) have been already included in the diffusional term δc_i^d, which is obtained by statistical averaging just over these short-wave fluctuations. This agrees with the fact that all quantities entering Eq. (56), including the mean site occupation c_i, the site chemical potentials λ_i, and the diffusional term δc_i^d, have a physical meaning only within some locally equilibrated region referred to in textbooks as "a quasi-closed subsystem" [1] containing a sufficiently large number of atoms. In other words, in our statistical description, which involves dividing

the whole nonuniform nonequilibrium alloy into locally equilibrated quasi-closed subsystems, we consider only "thermodynamic" fluctuations δn_{ij}^f that have approximately the same value (for all bonds ij of a given crystal orientation α) within each quasi-closed subsystem, while a nonzero fluctuative contribution to the total δc_i in (56) arises only due to a relatively weak nonuniformity of these fluctuations. Therefore, in the last term in Eq. (56), the full fluctuative transfer δn_{ij}^f should be replaced with its long-wave (or "coarse-grained") part δn_{ij}^{fc}. This last can be obtained by introducing a proper cut-off factor $F_c(\mathbf{k})$ in the Fourier component $\delta n_{f\alpha}(\mathbf{k})$ of the full fluctuation $\delta n_{ij}^f \equiv \delta n_\alpha^f(\mathbf{R}_{s\alpha})$, where $\mathbf{R}_{s\alpha}$ denotes the position of the ij bond center in the appropriate crystal sublattice α formed by these centers [20]:

$$\begin{aligned} \delta n_\alpha^{fc}(\mathbf{R}_{s\alpha}) &= \sum_{\mathbf{k}} \exp(-i\mathbf{k}\cdot\mathbf{R}_{s\alpha})\,\delta n_\alpha^f(\mathbf{k})\,F_c(\mathbf{k}), \\ \delta n_\alpha^f(\mathbf{k}) &= \frac{1}{N}\sum_{\mathbf{R}_{s\alpha}} \exp(i\mathbf{k}\cdot\mathbf{R}_{s\alpha})\,\delta n_\alpha^f(\mathbf{R}_{s\alpha}), \end{aligned} \tag{60}$$

where N is the total number of lattice sites (or atoms) in the crystal. The cut-off factor $F_c(\mathbf{k})$ can be taken in the simple Gaussian-like form, which for the BCC lattice is

$$F_c^{BCC}(\mathbf{k}) = \exp[-4g^2(1-\cos\varphi_1\cos\varphi_2\cos\varphi_3)], \tag{61}$$

where $\varphi_\nu = k_\nu a/2$, k_ν is the vector $\mathbf{k}$ component along the main crystal axis ν, and a is the BCC lattice constant.

At $g^2 \gg 1$, expression (61) is reduced to a Gaussian $\exp(-k^2l^2/2)$ with $l = ga$. Hence, the reduced length $g = l/a$ characterizes the mean size of locally equilibrated quasi-closed subsystems. Generally, it is the characteristic length of uniformity of the site chemical potentials λ_i, which for a single-phase state (before nucleation) coincides with the uniformity length for local concentrations c_i. Estimates of this size are discussed in Sec. 4.2 below.

4. MODELS AND METHODS OF SIMULATION

4.1. Alloy models and states used for simulations

In most of our simulations, we use the first-principle microscopic model of FeCu alloys suggested by SF [18]. This model describes well the available thermodynamic and kinetic data for such alloys. This is a model with the next-to-nearest-neighbor interaction based on *ab initio* density functional theory calculations using the SIESTA code. For this model, the configurational interactions v_n for the nth neighbors in (22), the kinetic interactions $u_n^{\mathrm{Cu}} \equiv u_n$ in (17), the saddle-point energy parameters Δ^p in (33), the activation energies E_{ac}^{pv} in (14) (all in eV), and the attempt frequencies ω_{pv} in (14) (in sec^{-1}) have the following values:

$$\begin{aligned} v_1 &= -0.121{+}0.182T, \quad v_2 = -0.021{+}0.091T, \\ u_1 &= 0.127{-}0.091T, \quad u_2 = 0.044{-}0.045T, \\ \Delta^{\mathrm{Cu}} &= 0.05, \quad \Delta^{\mathrm{Fe}} = -0.03, \\ E_{ac}^{\mathrm{Cu}_v} &= 0.438, \quad E_{ac}^{\mathrm{Fe}_v} = 0.698, \\ \omega_{\mathrm{Cu}_v} &= 5\cdot 10^{15}, \quad \omega_{\mathrm{Fe}_v} = 2\cdot 10^{15}. \end{aligned} \tag{62}$$

The second terms in the expressions for v_n and u_n phenomenologically describe the influence of anharmonic and magnetic effects. Our simulations for the SF model were mainly performed at the concentration $c = 0.0134$ and three temperatures 773, 713, and 663 K; these alloy states are respectively denoted as SF-1, SF-2, and SF-3. In Tables 1 and 2 in Sec. 5, we also present some results for the alloy state SF-4 that corresponds to $c = 0.0197$ and $T = 773$ K.

We also use two more models suggested by Le Bouar and Soisson [16] (LBS). The parameters of these models have been fitted to energies of configurations and vacancy migration barriers computed with the embedded atom method potential. The LBS-1 model is the nearest-neighbor interaction model with the following parameter values (in the same units as in (62)):

$$\begin{aligned} \text{LBS-1}: \quad v_1 &= -0.20, \quad u_1 = 0.155, \\ \Delta^{\mathrm{Cu}} &= \Delta^{\mathrm{Fe}} = 0, \\ E_{ac}^{\mathrm{Cu}_v} &= 0.018, \quad E_{ac}^{\mathrm{Fe}_v} = 0.64, \\ \omega_{\mathrm{Cu}_v} &= \omega_{\mathrm{Fe}_v} = 5\cdot 10^{15}. \end{aligned} \tag{63}$$

For the LBS-2 model, all parameters are the same as in (63) except the saddle-point energy parameter Δ^{Fe}, which is

$$\text{LBS-2}: \quad \Delta^{\mathrm{Fe}} = -0.238. \tag{64}$$

Our simulations for these two models were performed at $c = 0.01$ and $T = 1000$ K, and these alloy states are respectively denoted as LBS-1 and LBS-2.

Comparison of the SF and LBS models discussed in [18] (a more detailed comparison is given in Ref. [30]) shows that the SF model yields a lower solution energy of copper in BCC iron (which leads to the lower density and larger sizes of nucleating precipitates), and the larger difference between vacancy formation energies in pure BCC iron and pure BCC copper (which leads to a stronger vacancy trapping in copper precipitates and to

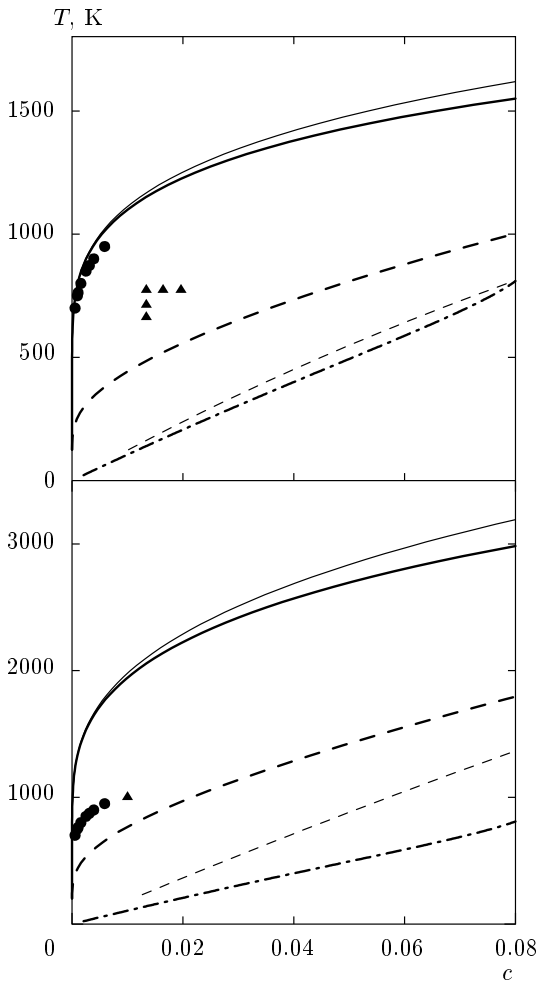

Fig. 1. Calculated phase diagrams for the SF model (upper figure) and the LBS model (lower figure). Thick lines correspond to the pair cluster approximation (PCA), and thin lines correspond to the mean field approximation (MFA); solid lines are binodals, and dashed lines are spinodals. Solid circles and the chained line show the binodal and spinodal calculated using the CALPHAD expression for the free energy of BCC FeCu alloys taken from [11]. Triangles indicate the (c, T) states used for simulations (color online [31])

a higher mobility of precipitates). As discussed by SF, the LBS models describe FeCu alloys less realistically than the SF model, but we consider these LBS models for methodological reasons, to follow the influence of variations of the coupling constants and saddle-point energy parameters on the precipitation kinetics.

Binodals and spinodals for the SF and LBS models calculated using the PCA, MFA, and CALPHAD expressions for the free energy are presented in Fig. 1, where we also show the initial alloy states used in our

Table 1. Alloy states used in our simulations

Model	SF				LBS-1,2
T, K	773	713	663	773	1000
c, at. %	1.34	1.34	1.34	1.97	1
s	0.285	0.352	0.425	0.426	0.459
Alloy state	SF-1	SF-2	SF-3	SF-4	LBS-1,2

simulations. These states are chosen in the metastable region $T_s(c) < T < T_b(c)$ or $c_b(T) < c < c_s(T)$ (where the subscript s or b corresponds to the spinodal or binodal), which corresponds to the nucleation and growth (NG) type of alloy decomposition. The degree of supersaturation for each of these states can be quantitatively characterized by the reduced supersaturation parameter s introduced in [28]:

$$s(c,T) = [c - c_b(T)]/[c_s(T) - c_b(T)]. \qquad (65)$$

Values $s < 1$ correspond to the NG, while $s > 1$, to the spinodal decomposition (SD) evolution type; the values of s for the alloy states studied are presented in Table 1.

To appreciate the accuracy of the results presented in Fig. 1, we first note that the PCA fully takes the pairwise correlations of atomic positions into account and neglects only many-particle ones [25]. Therefore, in the dilute alloy limit $c_i \to 0$, the PCA expressions for thermodynamic potentials become exact. In particular, free energy (24) in this limit takes the form

$$F_{PCA}\Big|_{c\to 0} = -\frac{1}{2}\sum_{ij} c_i c_j f_{ij}, \qquad (66)$$

which is just the discrete lattice analogue of the first term in the virial expansion of the free energy in powers of density (in our case, in powers of c_i) for the standard "weakly nonideal gas" theory [1]. Therefore, at low concentrations under consideration, we can expect the accuracy of all thermodynamic results of the PCA, including both binodals and spinodals, to be high, and we use the PCA for all thermodynamic calculations.

It follows from the upper frame of Fig. 1 that at relatively low c and T values used in our simulations, the binodals calculated using the PCA, MFA, or CALPHAD methods virtually coincide with each other. At the same time, the CALPHAD or MFA-calculated spinodals $c_s(T)$ exceed those found in the PCA (and hence the exact ones) by about a factor of 2. This leads to

Table 2. Parameters of the "thermodynamic" critical embryos for the alloy states considered

Alloy state	s	F_c/T	R_c, nm	ΔN_c	N_c
SM [4]	0.287	7.48	0.488	32.5	33.8
SF-1	0.285	4.38	0.417	13.3	14.3
SF-2	0.352	2.47	0.438	9.7	10.7
SF-3	0.425	1.36	0.468	7.2	8.2
SF-4	0.426	1.90	0.475	10.4	11.9
LBS-1,2	0.459	0.83	0.497	5.4	6.2

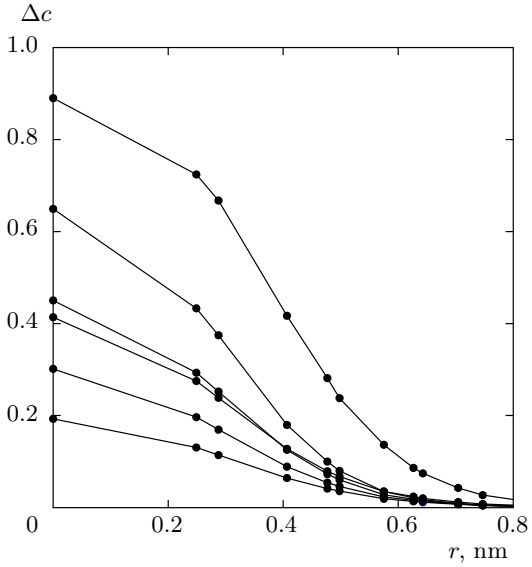

Fig. 2. Concentration profiles $\Delta c_i = c_i - c$ in thermodynamic critical embryos for the alloy states studied. Different curves from top down correspond to the states SM [4], SF-1, SF-2, SF-4, SF-3, and LBS (color online [31])

a strong underestimat ion of the reduced supersaturation $s(c,T)$, which should result in drastic distortions of microstructural evolution. Therefore, as mentioned in Sec. 1, using the phase–field-type methods based on CALPHAD or MFA expressions for thermodynamic potentials can hardly provide an adequate description of the alloy decomposition kinetics at low concentrations and temperatures under consideration.

Figure 2 illustrates the structure of "thermodynamic" critical embryos for the alloy states studied. This structure was calculated by the method in Ref. [27], mentioned in Sec. 3.1, with the use of the PCA. The figure shows, in particular, that the sizes of critical embryos in our problem are comparable to the host (BCC iron) lattice constant: $a_{\mathrm{Fe}} = 0.287$ nm, and therefore neglecting the discrete lattice effects made in the phase–field-type approaches can lead here to hard-to-control errors. In Table 2, we present main characteristics of these critical embryos: the reduced nucleation barrier F_c/T, the mean radius of the embryo R_c, the total excess ΔN_c of minority (copper) atoms in the embryo with respect to the initial state, and the total number N_c of minority atoms in the embryo. The barrier F_c is calculated in accordance with Eq. (4) in [28] (where it was denoted as $\Delta\Omega_c$), and the quantities R_c, ΔN_c, and N_c are defined by the relations

$$R_c^2 = \sum_i r_i^2 \frac{c_i - c}{\Delta N_c}, \quad \Delta N_c = \sum_i (c_i - c), \qquad N_c = \Delta N_c + cN_s^c. \tag{67}$$

The index i labels lattice sites, N_s^c is the total number of sites (atoms) in a precipitate, and the term cN_s^c describes the contribution of the "uniform background" minority atoms to N_c. For comparison, in Fig. 2 and Table 2, we also present the analogous results for the SM alloy state [4], which corresponds to the nearest-neighbor interaction with $v_1 < 0$, $T = 0.4(-v_1)$, and $c = 0.03$. We see that the N_c and F_c/T values for the realistic SF models are notably lower than for the SM model. Therefore, manifestations of fluctuations in nucleation processes for these realistic models should be much stronger than those for the simple SM model, which is illustrated in Secs. 5.1 and 5.3 below.

We now discuss the expressions for the effective mobilities M_{ij} in Eq. (45). The LBS-1 model corresponds to the configuration-independent saddle-point energies for which the correlators b_{ij}^p in (17) are independent of the species p of an atom. As mentioned in Sec. 2.3, adiabaticity equation (34) is then solved analytically, and the effective mobility $M_{ij} = M_{ij}^{\alpha h}$ is given by Eq. (39).

For two other models, SF and LBS-2, the saddle-point energies depend on configurations, and hence adiabaticity equation (34) can be approximately solved only if either of inequalities (43) is obeyed at c_i values significant for the kinetic process studied; for brevity, we let such c_i be denoted by c_s. We first consider NG-type processes for the SF model. The experience of our simulations for all models considered (illustrated by Figs. 20–22 below) shows that the local concentrations c_s that are significant for NG usually have the order $c_s \sim 0.1$. To estimate the products $\eta_i r_{ij}$ in Eqs. (43), we first consider the case where these c_s are small, and hence both functions $\ln(1 - g_{ij}c_j) \sim \ln(1 - f_{ij}c_s)$ in Eq. (20) and $(1 + \bar{c_{ij}} f^{Ap})^6 \sim \exp[6\ln(1 + c_s f^{Ap})]$ in Eq. (33) can be expanded in powers of c_s. Substituting

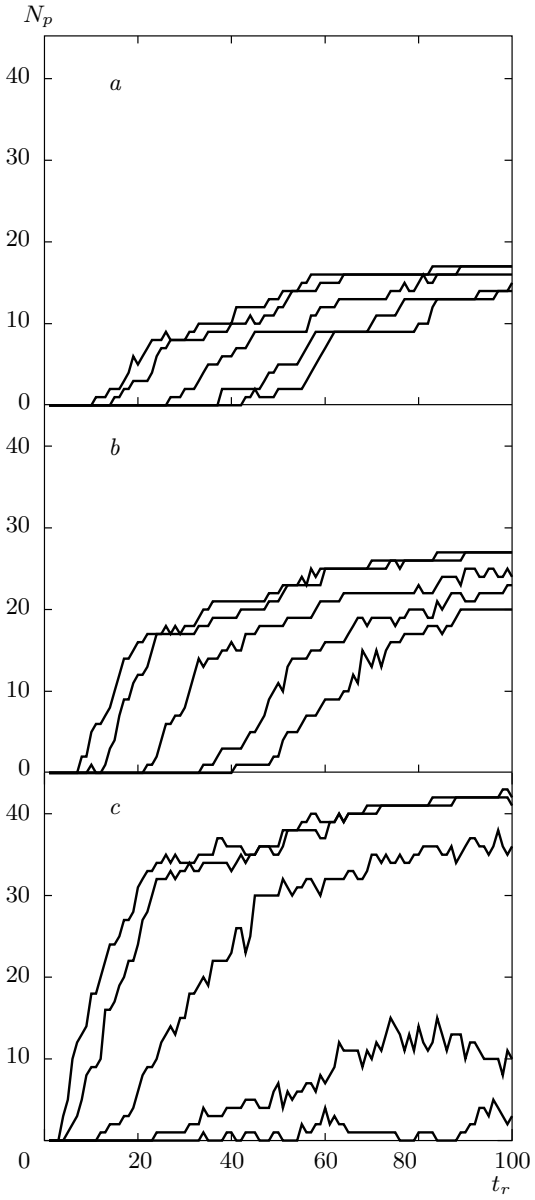

Fig. 3. The total number of precipitates that contain $i \geq p$ copper atoms, $N_p(t_r, g)$, versus the reduced time t_r defined by Eq. (51), obtained in SSA simulations with different g in Eq. (61) for the SF-1 state. Frames a, b, and c correspond to g equal to 1.75, 1.65, and 1.55, while different curves in each frame correspond to $p = 10$, 20, 40, 60, and 70 from left to right

numerical values of parameters (62) in these expansions, we obtain the following estimates of $\xi_{ij} = \eta_i r_{ij}$ for the SF-1 and SF-3 states:

$$\xi_{ij}^{SF-1} \sim 20 c_s \exp(80 c_s), \qquad \xi_{ij}^{SF-3} \sim 40 c_s \exp(160 c_s), \tag{68}$$

while for the SF-2 state, the ξ_{ij} value lies between these two estimates. For $c_s \gtrsim 0.1$, all these values much exceed unity. Therefore, inequality (b) in (43) is obeyed, and QKE (45) with the effective mobility M_{ij} given by Eq. (50) can be used for all our SF states.

To estimate the products $\xi_{ij} = \eta_i r_{ij}$ in Eqs. (43) for the LBS-2 state, we again expand the functions $\ln(1 - g_{ij} c_j) \sim \ln(1 - f_{ij} c_s)$ in (20) and $(1 + \bar{c_{ij}} f^{Ap})^6 \sim \sim \exp[6 \ln(1 + c_s f^{Ap})]$ in (33) in powers of c_s. Substituting numerical values of parameters from Eqs. (63), we then obtain

$$\eta_i r_{ij}^{LBS-2} \sim 1400 c_s \exp(-40 c_s). \tag{69}$$

At c_s between 0.01 and 0.1, the right-hand side of this estimate is large, inequality (b) in (43) is obeyed, and Eq. (50) for the effective mobility M_{ij} can be used; at $c_s \gtrsim 0.15$, this right-hand side is small, and Eq. (46) for M_{ij} can be used; and at c_s between 0.1 and 0.15, the right-hand side is of the order of unity, and therefore neither of inequalities (43) is obeyed. Therefore, the equivalence of the VME kinetics to that for DAE model (45) cannot be formally proved for the LBS-2 state, and we made no SSA simulations for this state. However, the above remarks enable us to suggest that such an equivalence probably exists, with the mobility M_{ij} in QKE (45) smoothly varying between expression (50) for $c_s < 0.1$ and expression (46) for $c_s > 0.15$. Then the precipitation kinetics for the LBS-2 state should be quite similar to that for the LBS-1 state, differing only by replacing the factor $b_{ij}^{\alpha} = b_{ij}$ in Eq. (46) for the LBS-1 state with some smaller factor varying between $b_{ij}^{h} < b_{ij}$ at $c_s < 0.1$ and $b_{ij}^{\alpha} = b_{ij}$ at $c_s > 0.15$. This should correspond just to some slowing down of precipitation kinetics for the LBS-2 state with respect to the LBS-1 state, and the KMCA results of LBS [16] seem to agree with these considerations.

In Table 3, to characterize the strength of configurational (or "thermodynamic") interactions v_n and the kinetic interactions u_n for the alloy states considered, we present the values of the Mayer functions f_n^v and of analogous "kinetic" functions f_n^u defined by

$$f_n^v = \exp(-\beta v_n) - 1, \quad f_n^u = \exp(\beta u_n) - 1, \tag{70}$$

as well as of the functions f_{Δ}^p in Eq. (33). The functions f_n^v enter Eqs. (20)–(24) for the site chemical potentials λ_i and the free energy F, while the functions f_n^u and f_{Δ}^p enter Eqs. (25)–(33), (39), (46), and (50) for the correlators b_{ij}^p and effective mobilities M_{ij}. In Table 3, we also present expressions for the correlators b_{ij}^{Fe} and the reduced effective mobilities $M_{ij}^r = M_{ij}/\gamma_{\alpha h}^{eff}$ in Eqs. (39), (46), and (50) at small $c_i \approx \bar{c}_{ij} \lesssim 1/f_1^v$,

Table 3. Values of the functions f_n^v, f_n^u, and f_Δ^p in Eqs. (70) and (33), and expressions for the correlators b_{ij}^{Fe} and reduced effective mobilities $M_{ij}^r = M_{ij}/\gamma_{\alpha h}^{eff}$ in Eqs. (39), (46), and (50) at small $c_i \approx \bar{c}_{ij} \lesssim 1/f_1^v$ for the alloy states studied

Alloy state	f_1^v	f_2^v	f_1^u	f_2^u	f_Δ^{Fe}	f_Δ^{Cu}	b_{ij}^{Fe}	M_{ij}^r
SF-1	4.1	0.3	5.2	0.9	5.8	24	$\exp(81c_i)$	$\exp(47c_i)$
SF-2	4.9	0.3	6.3	1.0	7.0	33	$\exp(98c_i)$	$\exp(57c_i)$
SF-3	5.9	0.3	7.5	1.1	8.5	43	$\exp(118c_i)$	$\exp(69c_i)$
LBS-1	9.2	0	5.0	0	5.0	5.0	$\exp(71c_i)$	$\exp(-3c_i)$

which have been mentioned to be most significant for the NG-type processes.

We discuss the results presented in Table 3. First, they show that both the thermodynamic and kinetic interactions for the alloy systems considered are rather strong: the f_1^v, f_1^u, and f_Δ^p values much exceed unity. This again shows that the MFA or CALPHAD-type expressions for thermodynamic and kinetic parameters based on the approximations $\beta v_n \ll 1$, $\beta u_n \ll 1$ [21] cannot be used to describe these alloy states. Second, the last column of Table 3 shows that the NG kinetics for the SF model should notably differ from that for the less realistic LBS-1 model. At the small local concentrations c_i considered, the reduced mobility M_{ij}^r for the LBS-1 model is virtually a constant close to unity, while for the SF model, it sharply increases with c_i and is typically very large. According to Eqs. (58) and (59), this mobility determines the scale of fluctuative terms in SKE (56). Therefore, we can expect the manifestations of fluctuation effects for the SF model to be much stronger than for the LBS-1 model. This agrees with the KMCA results presented in Figs. 11–14 below.

4.2. Estimating the local equilibrium length for the SSA

As discussed in Sec. 3.2, the reduced length $l = ga$ in SSA equations (60) and (61) characterizes sizes of locally equilibrium quasi-closed subsystems used in our statistical description of a nonequilibrium alloy. This length cannot be chosen smaller than the characteristic length l_{nu} of nonuniformity of local chemical potentials, which for the nucleation processes typically has the same order of magnitude as the critical embryo size R_c (see, e. g., Figs. 20–22 below). The actual distribution of local equilibrium lengths $l \lesssim l_{nu}$ in an alloy varies with both space and time; in particular, after creation of a supercritical precipitate, the degree of local equilibrium in the adjacent region should significantly increase with respect to other regions where such precipitates are not born yet.

For simplicity, we characterize the distribution of all local lengths l by a single spatially averaged parameter $\bar{l} = ga$, where the reduced length g, generally, varies with the evolution time t or the reduced time t_r in (51) used in the SSA. After completion of nucleation at some $t_r = t_r^N$, the alloy rapidly approaches the full two-phase equilibrium, and the length $\bar{l}$ should become large. Then the cut-off parameter $g = g(t_r)$ in Eq. (61) at $t_r \gtrsim t_r^N$ should also be large, the fluctuative terms δn_f in (56) become small, and SKE (56) transforms into QKE (45) with no fluctuation terms.

To describe the above-discussed physical picture with the minimal number of model parameters, we approximate the time dependence $g(t_r)$ by the simplest expression

$$\begin{aligned} t_r < t_r^N: &\quad g(t_r) = g_0, \\ t_r > t_r^N: &\quad g^2(t_r) = g_0^2 + (t_r - t_r^N) C D^{eff}, \end{aligned} \tag{71}$$

where D^{eff} is the effective reduced diffusivity, which can be estimated as $D^{eff} \approx \gamma_{\mathrm{FeCu}}^{eff}$ [32, 33] for direct-exchange model (45), and C is a numerical factor, e. g., $C = 2$ for the standard diffusion law. At $C \sim 1$, the evolution of microstructure was found to be virtually independent of the C value, and we usually put $C = 2$.

The simple model for $g(t_r)$ in (71) includes an unphysical break at $t_r = t_r^N$, which leads to the presence of analogous fictitious breaks in various characteristics of the evolution, e. g., in Figs. 4–7, 9, 10, and 15 below. In reality, as we have noted, the effective equilibrium length starts to increase immediately after the beginning of nucleation, and hence the function $g(t_r) = \bar{l}/a$ monotonically increases with time with no breaks. Therefore, for a more realistic description, some other model should be used for $g(t_r)$ that describes its continuous increase with t_r and the resulting smooth decrease of fluctuations in the course of

both nucleation and growth stages. But the experience of our simulations shows that at t_r not close to t_r^N, the main characteristics of microstructure, such as the density and sizes of supercritical precipitates, are not sensitive to the detailed form of $g(t_r)$ if the scale of this function is determined by the "maximum thermodynamic gain" principle described below. Therefore, in this work, we use the simplest form (71) for $g(t_r)$.

The parameter g_0 in Eq. (71) can be estimated in two ways. First, it can be found by fitting the SSA simulation results for the evolution of density of precipitates to the analogous KMCA results, for example, to those presented in Figs. 11–14 below. But such "KMCA-based" estimates of g_0 would limit possible applications of the SSA to the models for which reliable KMCA results are available. To estimate g_0 within the SSA, we can try to extend the second law of thermodynamics, that is, the principle of the free energy minimum with respect to all its free parameters, which is valid for equilibrium systems, to the kinetic processes in the nonequilibrium systems studied. For this, we note that the main characteristics of microstructure formed in the course of the nucleation process, such as the characteristic nonuniformity length $l_{nu} \sim \bar{l}$, can be considered "free" parameters of a nonequilibrium state analogous to "static" free parameters for equilibrium systems. It therefore seems natural to suggest that the kinetic path of evolution of this nonequilibrium state should correspond to the maximum thermodynamic gain, that is, to the maximum rate of decrease in free energy. This suggestion can extend the "excess entropy production" approach to thermodynamics of irreversible processes discussed by Prigogine and coworkers [34] to the kinetics of essentially nonuniform and nonequilibrium systems under consideration. Then the characteristic value $l_{nu} \sim g_0 a$ can be estimated from the condition of the maximum thermodynamic gain in the course of the nucleation process, which in our model (71) corresponds to the minimum of the free energy $F(g_0, t_r \lesssim t_r^N)$ with respect to g_0.

This maximum thermodynamic gain should evidently correspond to the formation of the maximum number of large supercritical precipitates. At the same time, the density d_p of such precipitates sharply depends on the effective size $\bar{l}$ of quasi-equilibrium systems for the nucleation process. When $g = \bar{l}/a$ is too large, the fluctuations are too weak to overcome nucleation barriers, while when g is too small, the fluctuations are too strong to allow formation of large and steadily growing precipitates. Therefore, the dependences $d_p(g)$ should have a pronounced maximum at some optimal $g = g_0$. These considerations are illustrated by Fig. 3, where we present time dependences of the total number $N_p(t_r, g)$ of precipitates containing $i \geq p$ copper atoms obtained in the SSA simulations with different g. The "end of nucleation" time t_r^N here and below is defined as the time of creation of the last "critical" precipitate with $p \geq p_c$; these p_c values (which for the SF alloy states are close to the N_c values in Table 2) are estimated in Sec. 5.1. This definition of t_r^N is somewhat arbitrary, but it makes virtually no effect on the simulation results. For the evolution shown in Fig. 3*a*, the fluctuations seem to be too weak, and therefore the length $\bar{l} = ga$ is too large. For Fig. 3*c*, the fluctuations are evidently too strong, which leads to an unphysical evolution of large precipitates: they do not grow, in disagreement with the second law of thermodynamics; therefore, the g value here is too small. Finally, for the evolution shown in Fig. 3*b*, the g value seems to be close to optimum.

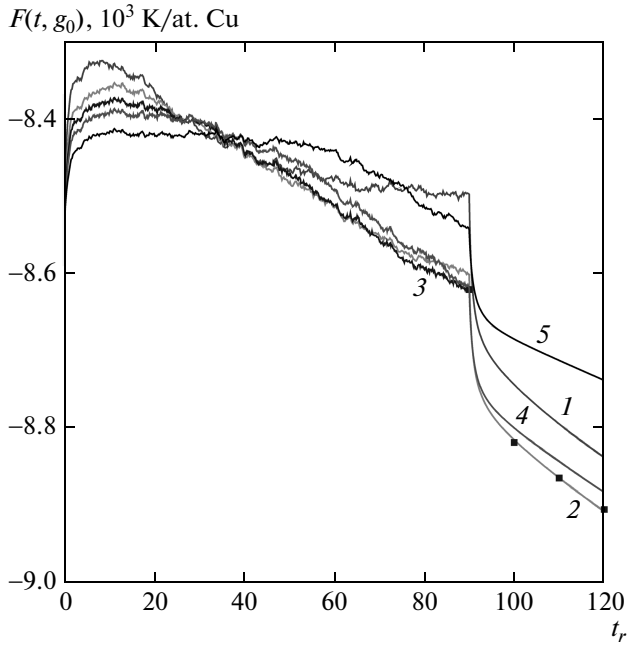

Fig. 4. Time dependence of the free energy per copper atom, $F(t_r, g_0)$, obtained in SSA simulations with different g_0 for the SF-1 state. Curves *1*, *2*, *3*, *4*, and *5* respectively correspond to $g_0 = 1.55$, 1.65, 1.7, 1.75, and 1.85 (color online [31])

In Figs. 4–7, we present time dependences of the free energy per copper atom, $F(t_r, g_0)$, obtained in the SSA simulations with different g_0 in Eq. (71). For definiteness, the initial state for these simulations was taken uniform: $c_i(0) = c = \text{const}$, and hence the initial increase in F at $t_r \lesssim 0.1 t_r^N$ is related just to switching

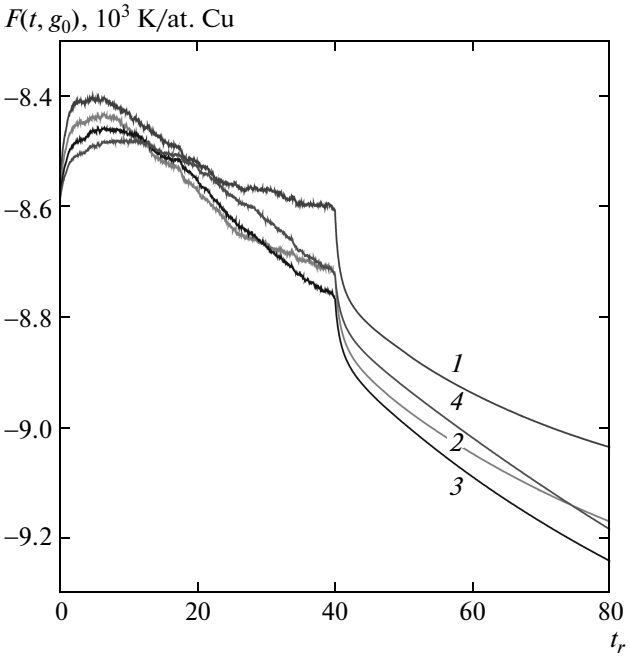

Fig. 5. The same as in Fig. 4, but for the SF-2 state. Curves *1*, *2*, *3*, and *4* respectively correspond to $g_0 = 1.6$, 1.7, 1.8, and 1.9 (color online [31])

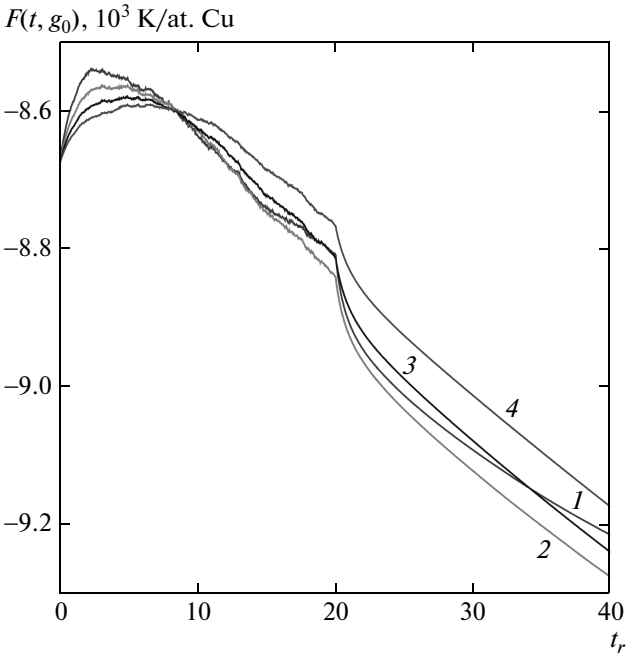

Fig. 6. The same as in Fig. 4, but for the SF-3 state. Curves *1*, *2*, *3*, and *4* respectively correspond to $g_0 = 1.8$, 1.9, 2, and 2.1 (color online [31])

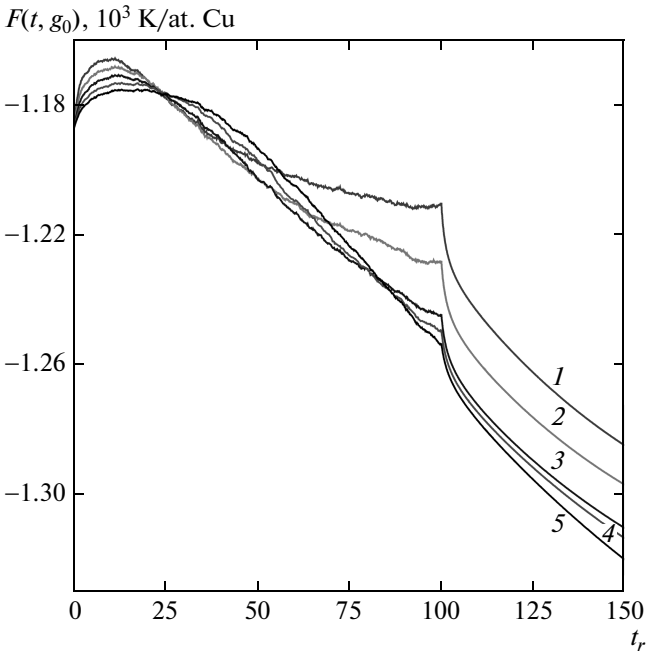

Fig. 7. The same as in Fig. 4, but for the BS-1 state. Curves *1*, *2*, *3*, *4*, and *5* respectively correspond to $g_0 = 1.7$, 1.8, 1.9, 2, and 2.1 (color online [31])

on fluctuations at $t_r = 0$ and has no physical meaning. At $t_r \approx t_r^N$, the functions $F(t_r, g_0)$ show the above-mentioned fictitious breaks due the analogous breaks in our model functions $g(t_r)$ in (71). But at t_r not close to zero or to t_r^N, e. g., at $t_r \approx 0.5t_r^N$, the functions $F(t_r, g_0)$ presented in Figs. 4–7 can be realistic. Therefore, the "optimal" g_0 value can be estimated from comparison of these functions at $t_r \sim 0.5t_r^N$ for different g_0.

Figures 4–7 show that these functions have a distinct minimum at a certain g_0 for each alloy state considered. For the SF-1 state, this minimum corresponds to g_0 equal to 1.65 or 1.7; for the SF-2 state, to $g_0 = 1.7$ or 1.8; for the SF-3 and LBS-1 states, to $g_0 = 1.9$ or 1.8. The first values seem to be slightly more appropriate, but using the second values in simulations changes results only slightly; this is illustrated below for the SF-2 model. For the reduced length g_0 in Eq. (71), we therefore use the values

$$g_0^{SF-1} = 1.65, \quad g_0^{SF-2} = 1.7, \\ g_0^{SF-3} = 1.9, \quad g_0^{LBS-1} = 1.9. \tag{72}$$

The minimum local equilibrium lengths $l_0 = g_0 a$ for these g_0 have the same order of magnitude as the critical sizes R_c in Table 2, in accordance with the considerations mentioned above.

We comment on the loss of validity of the SSA at low g, which is manifested, in particular, in the above-mentioned unphysical results presented in Fig. 3*c*. This problem was discussed in detail by SPV in [20], who noted that the statistical approach, in particular, used basic equations (9)–(13) that include averaging over locally equilibrated quasi-closed subsystems, which implies that the reduced size g of these subsystems is not too small, and hence they include a sufficiently large number of atoms, while the site chemical potentials λ_i in these subsystems should obey the local equilibrium condition $\lambda_i \approx$ const. The scale of violations of this basic condition can be characterized by the "parameter of nonequilibrium" J introduced by SPV:

$$J(g, t_r) = \frac{1}{N_b} \sum_{i,j} |\lambda_i - \lambda_j|/T, \qquad (73)$$

where N_b is the total number of the nearest-neighbor bonds $\{ij\}$ and the sum is taken over all such bonds in an alloy. In Fig. 8, we show the values of this parameter averaged over the incubation stage, $J_{inc}(g) = \langle J \rangle_{inc}$; for different alloy states, the functions $J_{inc}(g)$ are similar. At small $g \lesssim 1.5$, these functions start to sharply increase, which reflects sharp violations of statistical equilibrium within too small quasi-closed subsystems. But for the $g = g_0$ values presented in Eqs. (72), this parameter is still small: $J_{inc}(g) \sim 0.1$—0.15, and hence using the SSA seems to be justified.

In Fig. 9, we show time dependences of nonequilibrium parameter (73) at first stages of the evolution. As mentioned, breaks in the $J(t_r)$ curves at $t_r = t_r^N$ are due to the similar breaks in our simple model (71); for more realistic models mentioned above, these breaks should be replaced by some smooth decrease in $J(t_r)$ at $t_r \gtrsim 0.5 t_r^N$. The increase in $J(t_r)$ after the beginning of nucleation is related to the occurrence of interfaces and spacial nonuniformities, which lead to some additional, "nonuniform" contributions to the differences $|\lambda_i - \lambda_j|$ in Eq. (73). The decrease in $J(t_r)$ after the completion of nucleation is due to the increase in the local equilibrium length $g(t_r)$ at $t > t_r^N$ mentioned in the discussion of model (71). It leads to a sharp decrease in the fluctuative terms δn_f in SKE (56), and hence the degree of local equilibrium in the system sharply increases.

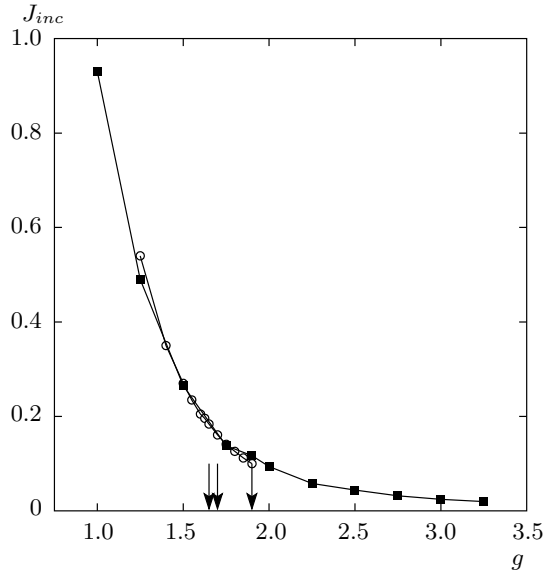

Fig. 8. Parameter of nonequilibrium (73) for the incubation stage observed in SSA simulations with different reduced lengths g. Circles and squares respectively correspond to the SF-1 and LBS-1 states. Arrows indicate g_0 values in Eqs. (72) (color online [31])

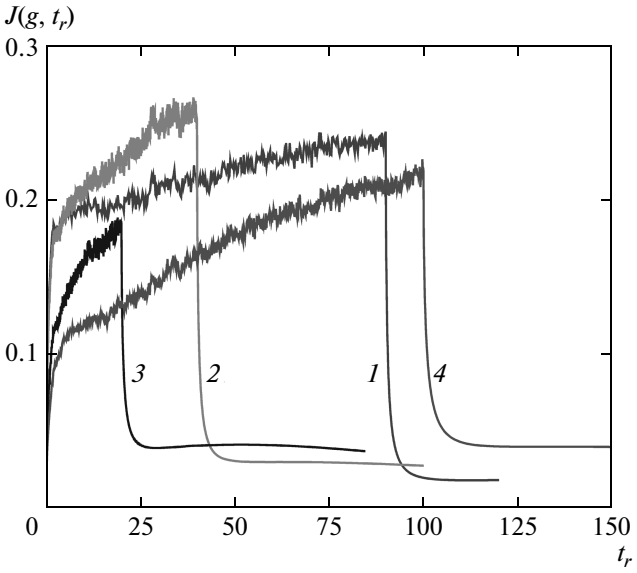

Fig. 9. The parameter $J(g, t_r)$ in (73) observed in the SSA simulations with $g = g_0$ from (72). Curves *1*, *2*, *3*, and *4* respectively correspond to the SF-1, SF-2, SF-3, and LBS-1 alloy states (color online [31])

4.3. Methods of KMCA simulations

The KMCA used in this study is described in detail in Refs. [16, 18]. We only recall the physical principles of the method, underlining the difference from the SSA. The KMC simulations follow the evolution of the atomic configuration in a simulation box of $N = 64^3$

lattice sites containing Fe and Cu atoms and one vacancy, with periodic boundary conditions. At each Monte Carlo step, 8 atom–vacancy exchanges between nearest-neighbor sites can occur in a BCC lattice, with the jump frequencies W_{ij}^{pv} given by Eq. (6). The activation energies are exactly computed for each local configuration, without using any mean field approximation. One of these exchanges is chosen, using a pseudo-random generator, by means of a residence time algorithm [35]. The physical time of the Monte Carlo simulation is given by

$$t_{MCS} = 1 \Big/ \sum_{j=1}^{8} W_{ij}^{pv}, \tag{74}$$

where the sum ranges over the 8 possible jumps. This time must be rescaled to take the real vacancy concentration into account, which depends on the precipitation microstructure. If we assume that the vacancy concentration remains at equilibrium in the different phases during all the precipitation, a convenient way to perform this time rescaling is

$$t = t_{MCS} \frac{c_V^{MC}(\mathrm{Fe})}{c_V^{eq}(\mathrm{Fe})}, \tag{75}$$

where $c_V^{eq}(\mathrm{Fe})$ is the equilibrium vacancy concentration in pure iron and $c_V^{MC}(\mathrm{Fe})$ is the vacancy concentration in copper-free regions of the KMC simulation box [16, 18]. The number N_p of copper-rich precipitates and their average size $\langle i \rangle$ (discussed in Sec. 5.1) are computed by considering only clusters that contain $i \geq p$ copper atoms connected by at least one nearest-neighbor bond.

4.4. Methods of SSA simulations

All SSA simulations were performed in a cubic box containing $N = 2 \times (64)^3$ BCC lattice sites with periodic boundary conditions. In describing precipitates, the precipitate containing $i \geq p$ copper atoms is defined as a set of adjacent sites i (connected by at least one bond) whose mean occupations c_i exceed a certain cut-off value: $c_i \geq c_{cut}$, while this set contains not less than p copper atoms:

$$N_{\mathrm{Cu}} = \sum_i c_i \geq p. \tag{76}$$

The choice of c_{cut} was found to be not essential, and for definiteness we took it the same as in experimental studies [7]: $c_{cut} = 0.05$.

In solving SKE (56) with diffusion term (57), we should take into account that this term is proportional to the generalized mobility M_{ij} times the factor $2\,\mathrm{sh}[\beta(\lambda_i - \lambda_j)/2] \approx \beta(\lambda_i - \lambda_j)$ describing a thermodynamic driving force, while the mobilities M_{ij} given by Eqs. (46) or (50) are proportional to the correlator b_{ij}^{α} or b_{ij}^{h} that very sharply increases with the local concentrations c_i; this last fact is illustrated by Eq. (33) and the last two columns in Table 3. These very sharp dependences do not allow using the standard iterative methods, such as the Euler or Runge–Kutta ones, for solving the SKE: after several iterations, the product $M_{ij}\beta(\lambda_i - \lambda_j)$ becomes so large that the time step needed to achieve numerical stability becomes too small for these algorithms to be used. On the other hand, there is no physical reason for the diffusion term to be too large, because the high mobility M_{ij} should lead to a very fast approach to the local equilibrium, at which local chemical potentials of adjacent sites, λ_i and λ_j, are very close to each other. In reality, therefore, diffusion terms (57) remain reasonably small. The problem with the application of standard iterative methods arises due to their discrete nature; numerical values of the differences $|\lambda_i - \lambda_j|$ cannot catch up with a very fast increase in b_{ij}, and the fictitious increase in their product occurs.

To overcome this methodological difficulty, we put restrictions on b_{ij} in our iterative computations, by setting it to not exceed a certain value b_{ij}^{max}: $b_{ij} \leq b_{ij}^{max}$. Then we made simulations with different b_{ij}^{max}, from smaller to larger ones, until all physically important characteristics of the evolution, including the incubation and nucleation times t_r^{inc} and t_r^N and the maximum density of supercritical precipitates d_s^{max}, ceased to significantly change as b_{ij}^{max} increases. This happens at $b_{ij}^{max} = 250$, and this value was used in all our simulations. Actually, at $b_{ij}^{max} = 500$, the d_s^{max} values may be even lower than at $b_{ij}^{max} = 250$ (while for $b_{ij}^{max} < 250$, they monotonically increase with b_{ij}^{max}), but the differences lie within statistical errors. After the nucleation stage is over and fluctuations are switched off according to model (71), the values $|\beta(\lambda_i - \lambda_j)|$ typically decrease by two orders of magnitude with respect to the nucleation stage. This allows us to significantly decrease b_{ij}^{max}, usually down to $b_{ij}^{max} = 10$, and thus to increase the time step in solving equations. Again, we checked that using the same b_{ij}^{max} equal to 250 both before and after t_r^N, and reducing it at $t_r > t_r^N$ down to $b_{ij}^{max} = 10$, leads to the same description of evolution. In our case, using the Runge–Kutta method does not improve the stability of the numerical solution of the equations, but requires more calculations at each integration step, and we therefore used the simpler Euler method in our simulations.

The computational efficiency of the SSA exceeds

that of the KMCA, mainly due to the reduction of the vacancy-mediated kinetics to the direct-atomic-exchange models described in Sec. 2.3. This allows simulating a much lower number of atomic exchanges than the number of vacancy jumps in the KMCA [18], which significantly reduces the computation time. For example, for precipitation in the SF model up to the coarsening stage with decreasing the precipitate density by about two times, the SSA computation times in our simulations are by an order of magnitude shorter than the KMCA computation times, even for the simple SSA codes used with no parallelization. Parallelization of these SSA codes (which is now underway) should further accelerate such computations, by at least an order of magnitude.

We finally discuss the rescaling of the reduced time t_r used in the SSA to the physical time t determined by Eq. (52). In accordance with the remarks at the end of Sec. 2.3, we suppose the effective mean time of direct atomic exchanges, $\tau_{\alpha h}^{eff}$ in (52), to be constant before and after nucleation (that is, for both $t_r < t_r^{inc}$ and $t_r > t_r^N$), and to linearly vary with t_r in the course of nucleation:

$$\tau_{\alpha h} = \begin{cases} a_1, & t_r < t_r^{inc}, \\ a_1 + (a_2 - a_1)\dfrac{t_r - t_r^{inc}}{t_r^N - t_r^{inc}}, & t_r^{inc} \le t_r \le t_r^N, \\ a_2, & t_r > t_r^N. \end{cases} \qquad (77)$$

The constant $a_1 = t_{inc}/t_r^{inc}$ is the ratio of the physical and reduced incubation times, while the constant a_2 can be estimated from the fit of the SSA simulation results to the evolution rate at the coarsening stage. Thus, model (77) includes only two parameters, t_{inc} and a_2, which can be estimated either from comparison to KMC simulations or from experiment.

In this paper, we use the KMCA results described below for such estimates. The resulting time rescaling is presented in Fig. 10 as the dependence of the effective direct exchange rates $\gamma_{\alpha h}^{eff}$ in Eq. (51) (to be abbreviated to γ^{eff}) on the physical time t; this dependence has a clearer physical meaning than $\tau_{\alpha h}(t_r)$ in Eq. (77). The results presented in Fig. 10 and in analogous Fig. 3 in [22] clearly illustrate the decisive role of vacancy trapping for time dependences of the effective direct exchange rates. For all models considered, these rates monotonically increase with the evolution time t, which reflects the development of vacancy trapping in the course of precipitation. For the BV model, this trapping is relatively weak, and γ^{eff} increases to the coarsening stage just by about a factor of two. For the LBS model, the vacancy trapping is also not too pronounced (although stronger than for the BV model), and the total increase in γ^{eff} is about 6 times. For the more realistic SF model, the vacancy trapping is very strong [18]. Therefore, for the three SF states considered, the γ^{eff} values increase between the incubation and nucleation stages by more than two orders of magnitude, and as the temperature T decreases, this increase seems to become greater, in accordance with a probable stronger trapping at lower T.

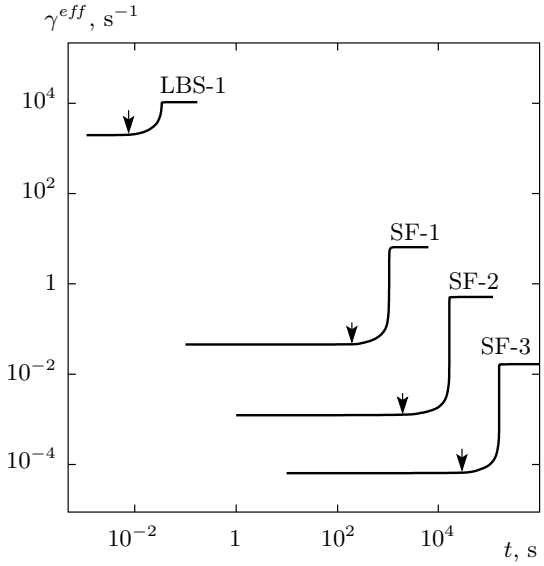

Fig. 10. Time dependence of the effective direct exchange rate $\gamma_{\mathsf{CuFe}}^{eff}$ in Eq. (41) estimated from comparison to the KMCA results. Different curves from top down respectively correspond to the alloy states LBS-1, SF-1, SF-2, and SF-3. Arrows indicate the incubation time t_{inc} (color online [31])

5. MICROSTRUCTURE EVOLUTION OBSERVED IN KMCA AND SSA SIMULATIONS

5.1. Evolution of density and sizes of precipitates

Evolution of the density of different precipitates is shown in Figs. 11–14. Solid lines and symbols in these figures show the results obtained in two different KMC runs; the differences between these lines and the symbols illustrate the scale of errors (mainly statistical) of these KMC results. It can be seen from Fig. 11 that for the SF-1 state and relatively small precipitates $p \lesssim 10$, such errors are significant at the nucleation stage, while

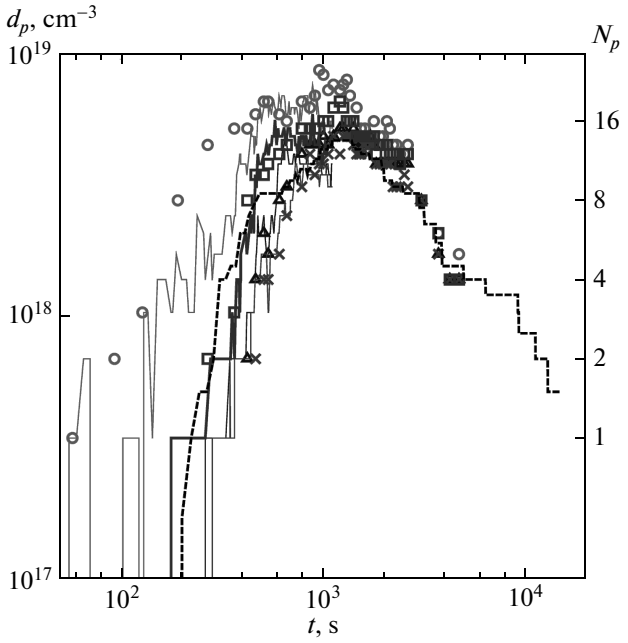

Fig. 11. Evolution of the density of precipitates containing $i \geq p$ copper atoms, d_p (left scale), and the total number of such precipitates within the KMC simulation box V_s^{KMC}, $N_p = N_p^{KMC}$ (right scale), for the SF-1 alloy state. For the SSA simulations with $V_s^{SSA} = 2V_s^{KMC}$, these N_p should be doubled: $N_p^{SSA} = 2N_p$. Solid lines from top down correspond to the respective KMCA results for $p = 11$, 15, 21, and 26, while the symbols (circles, squares, triangles, and crosses) show the analogous results obtained in another KMC run. The dashed line shows the SSA results for $p = 15$ and $g_0 = 1.65$ (color online [31])

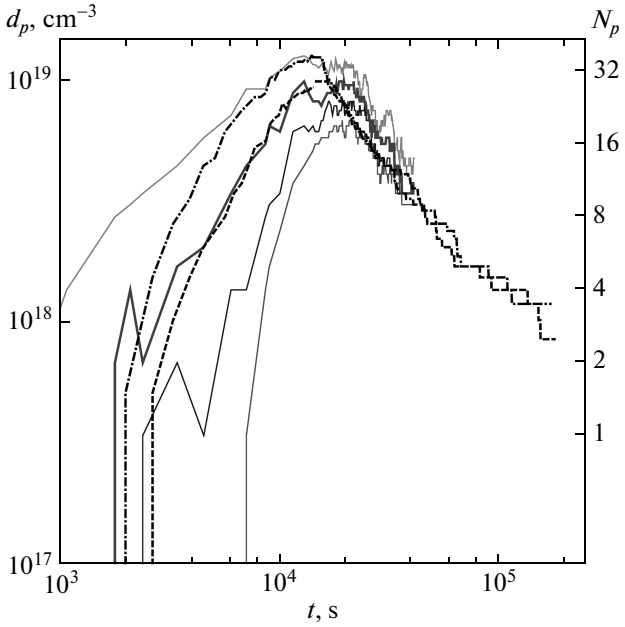

Fig. 12. The same as in Fig. 11, but for the SF-2 state and $p = 8$, 11, 16, and 21. The dashed curve shows the SSA results for $p = 11$ and $g_0 = 1.7$, and the chained line, the SSA results for $p = 11$ and $g_0 = 1.8$ (color online [31])

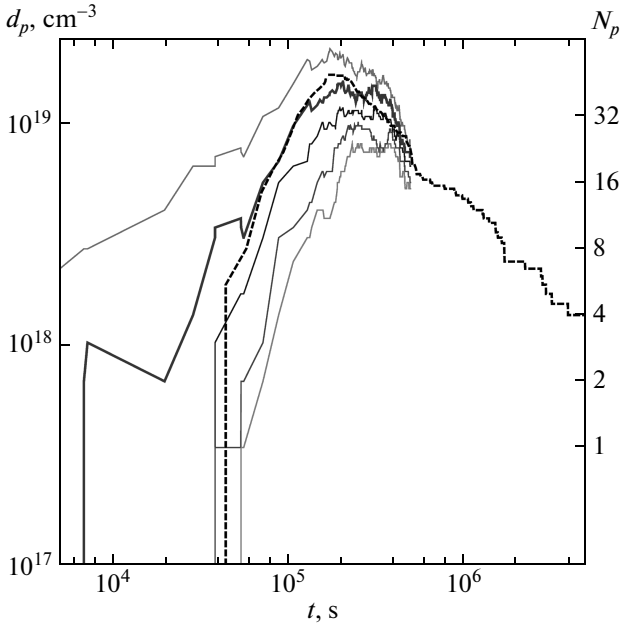

Fig. 13. The same as in Fig. 11, but for the SF-3 state and $p = 6$, 8, 11, 16, and 21, while the dashed curve shows the SSA results for $p = 8$ and $g_0 = 1.9$ (color online [31])

for larger p, and at later stages of the evolution, these errors decrease. For the LBS-1 model (Fig. 14), the differences between two KMC runs are smaller because the fluctuation effects are much weaker here. We also note that the difference between the values of d_p at two neighboring curves in Figs. 11–14, $d(i) = (d_{p_1} - d_{p_2})$, has the meaning of the density of precipitates that include i copper atoms with $p_1 \leq i < p_2$.

We first discuss the KMCA results presented in Figs. 11–14. We note that they qualitatively agree with the classical nucleation theory (CNT) ideas described in Sec. 3.1. In particular, all dependences $d_p(t)$ reveal the presence of four main stages of decomposition: incubation, nucleation, growth, and coarsening. For a more quantitative comparison to the CNT, we should estimate the "critical" embryo size p_c. In thermodynamic calculations in [26–28], the critical embryo is precisely defined as the set of mean occupations $\{c_i\}$ that

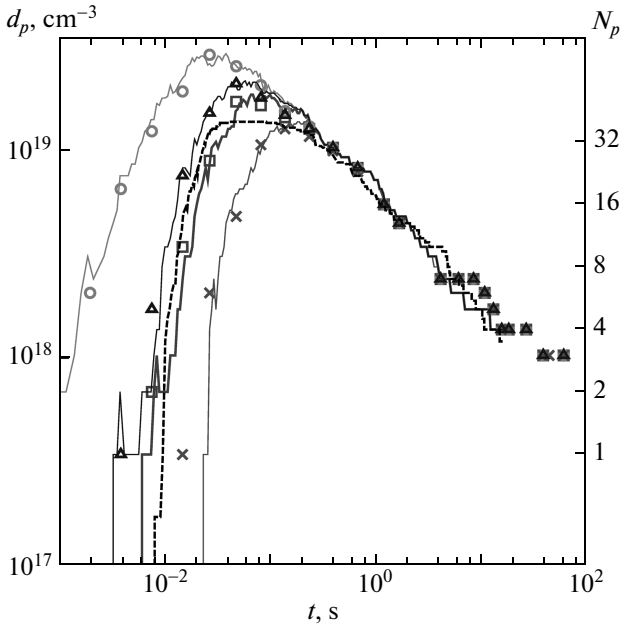

Fig. 14. The same as in Fig. 11, but for the LBS-1 state and $p = 6$, 11, 15, and 26, while the dashed curve shows the SSA results for $p = 15$ and $g_0 = 1.9$ (color online [31])

corresponds to a saddle point of the generalized free energy $F\{c_i\}$ in the multi-dimensional space c_i [27]. At the same time, the analogous critical size for nucleating precipitates cannot be defined uniquely. It seems natural to define it as the lowest value of the embryo size p such that the most probable evolution path at $p > p_c$ is growth rather than shrinkage or dissolution, but due to the presence of fluctuations inherent to the nucleation process, such "kinetic" critical sizes can be determined only approximately.

Using the KMCA results in Figs. 11–14, we can estimate these p_c from the shape of the $d_p(t)$ curves at different p. For the SF model, for which fluctuations in the dependences $d_p(t)$ are pronounced at small p and decrease at larger p, we can suggest that the beginning of decrease in these fluctuations with increasing p should correspond to the relation $p \gtrsim p_c$. For the SF-1, SF-2, and SF-3 states, this corresponds to $p_c \approx 15$, $p_c \approx 11$, and $p_c \approx 8$. Because these estimates agree well with the "thermodynamic" critical sizes N_c in Table 2, we use the respective values 15, 11, and 8 for the critical size p_c in the SF-1, SF-2, and SF-3 alloy state. We note that in the SSA simulations, the p_c values are used only to define the "end of nucleation" time t_r^N in Eq. (71) as the time of creation of the last critical precipitate, and slight variations of p_c have almost no effect on the evolution.

It can be seen from Figs. 11–13 that the time dependences $d_p(t)$ at these $p = p_c$ generally have a common form similar to that obtained by SM [4] in their simplified model, which agrees with the CNT ideas described in Sec. 3.1. At the same time, these dependences reveal at least two differences from the CNT ideas.

(A) Fluctuations in the $d_{p_c}(t)$ dependences are rather pronounced and significant even for "supercritical" embryos with $p > p_c$, and the more so for undercritical ones with $p < p_c$. This is especially clearly seen from the KMC results shown in Fig. 11 by solid lines, while in Figs. 12 and 13, these fluctuations are partly smoothed because fewer results are plotted.

(B) These fluctuations are large and important not only during the nucleation but also after its completion when the average density of supercritical precipitates ceases to increase. This is seen, in particular, in Fig. 13, where the curve $d_p(t)$ at $p = 16 \approx 2p_c$ reveals a wide and pronounced minimum between $t = 3 \cdot 10^5$ and $4 \cdot 10^5$ s, decreasing there by about 1.5 times. Therefore, for the SF model, fluctuations are important for the evolution even at the growth stage.

A thorough comparison of the KMCA results in Figs. 11–13 with the available measurements of the density of precipitates under decomposition of iron–copper alloys was made by SF [18]. It was found that the theory agrees with these experiments within the accuracy of both of them. According to Figs. 11–13, the same can also be said about the SSA results.

We now discuss the dependences $d_p(t)$ for the LBS-1 state, for which the thermodynamic nucleation barrier F_c (given in Table 2) is low, $F_c \lesssim T$. In this case, the evolution of not large "thermodynamically supercritical" embryos with $p \gtrsim N_c$ again differs from the CNT ideas: the effects of fluctuations are strong here due to the low thermodynamic gain under growth of such embryos. Because their stability is low, they often dissolve rather than steadily grow as the CNT supposes. This can qualitatively explain a significant decrease in the "plateau" in the $d_p(t)$ curves with $p \geq 15$ compared to those with $p = 6$ and $p = 10$ in Fig. 14. In this case, it seems more adequate to suppose the kinetic critical size p_c to significantly exceed N_c, such that the dominant evolution path at $p > p_c$ would be the growth of the embryo. For the LBS-1 state, we estimate this size as $p_c \approx 15$.

The SSA results for the precipitate density $d_p(t)$ presented in Figs. 11–14 have been obtained as described in Sec. 4. We note that a rescaling of the time t_r used in the SSA to the time t used in the

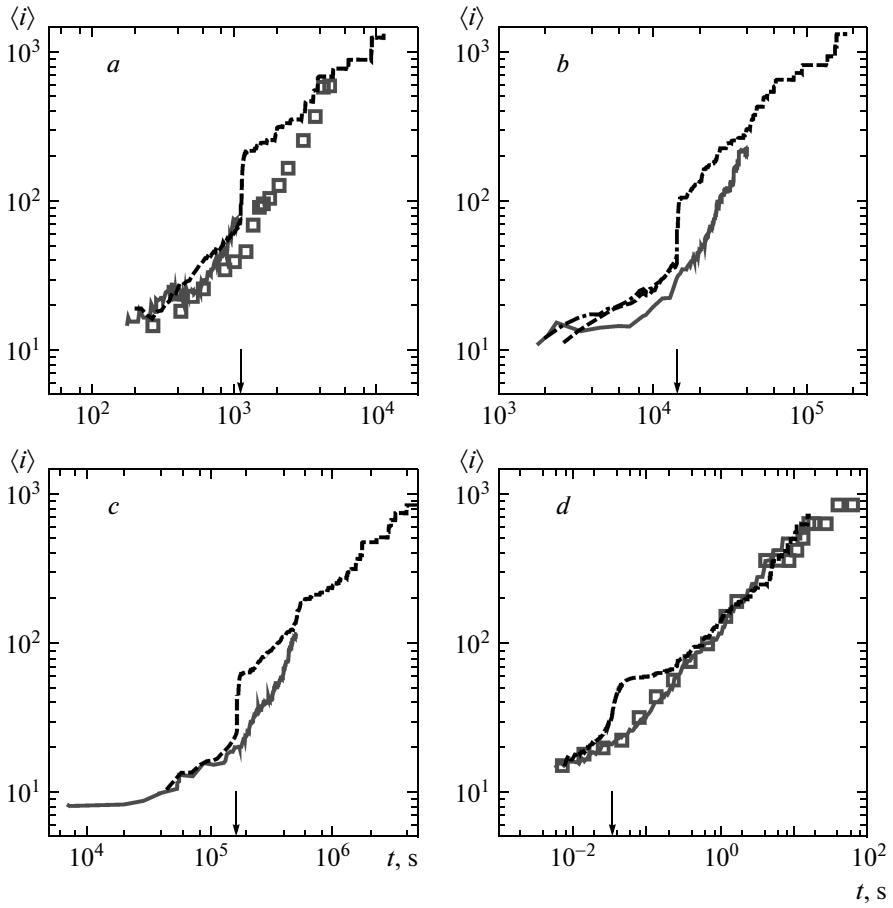

Fig. 15. The average number of copper atoms $\langle i \rangle$ within a precipitate versus the evolution time t. Frames a, b, c, and d correspond to the respective alloy states SF-1, SF-2, SF-3, and LBS-1. Solid lines and squares correspond to the KMCA. Dashed lines correspond to the SSA with g_0 from (72), and the chained line (in frame b), to $g_0 = 1.8$. Arrows show the t values that correspond to t_r^N in Eq. (71) (color online [31])

KMCA (illustrated by Fig. 10) corresponds to the above two-parametric fit of only the "horizontal" intervals in Figs. 11–14, while the "vertical" intervals, that is, the density d_p values, are calculated in the SSA with no fitting parameters. We see that for all the four alloy states considered, these $d_p(t)$ agree with the KMCA results within errors of these results mentioned above. Figure 12 (as well as Fig. 15b) also shows that changes in the SSA results due to possible variations of g_0 between $g_0 = 1.7$ and $g_0 = 1.8$ mentioned in deriving estimates (72) are relatively small.

In Fig. 15, we show time dependences of the average number of copper atoms within a precipitate ("precipitate size") $\langle i \rangle = i_p(t)$. Results of the KMCA and SSA calculations usually seem to agree within the KMCA errors except for time intervals just after t_r^N, where i_p^{SSA} notably exceed i_p^{KMCA}. This disagreement seems to be again related to crudeness of the oversimplified model (71) for the length $g(t_r)$ determining the scale of fluctuative terms δn_f in stochastic equation (56). As mentioned, model (71) corresponds to a constant $g(t_r) = g_0$ at $t_r < t_r^N$ and to a sharp increase in g (and hence to abruptly switching off the fluctuations) at $t_r \geq t_r^N$, while actually the length g starts to increase (and the fluctuations δn_f to decrease) immediately after the beginning of nucleation, and g remains finite (and fluctuation effects noticeable) at the growth stage as well. Therefore, at $t_r > t_r^N$, the SSA-calculated $i_p(t)$ in Fig. 15 grow more rapidly than in the KMCA (and in reality) because this growth is actually still hampered by noticeable fluctuation effects. Therefore, we can expect that these disagreements will reduce or vanish if the models of $g(t_r)$ more realistic than (71) are used in the SSA.

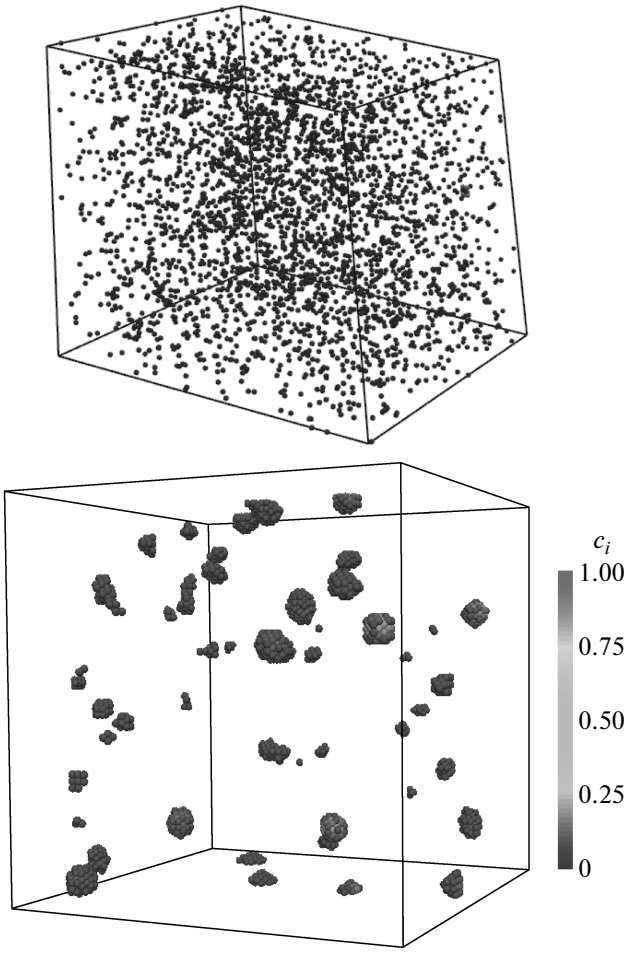

Fig. 16. Upper frame: Distribution of copper atoms for the SF-1 alloy state just before nucleation, $t = 55$ s, observed in the KMCA. Each sphere corresponds to a copper atom. Lower frame: Distribution of the local concentrations c_i for the same state as in the upper frame observed in the SSA. Sites with $c_i < 0.05$ are not shown (color online [31])

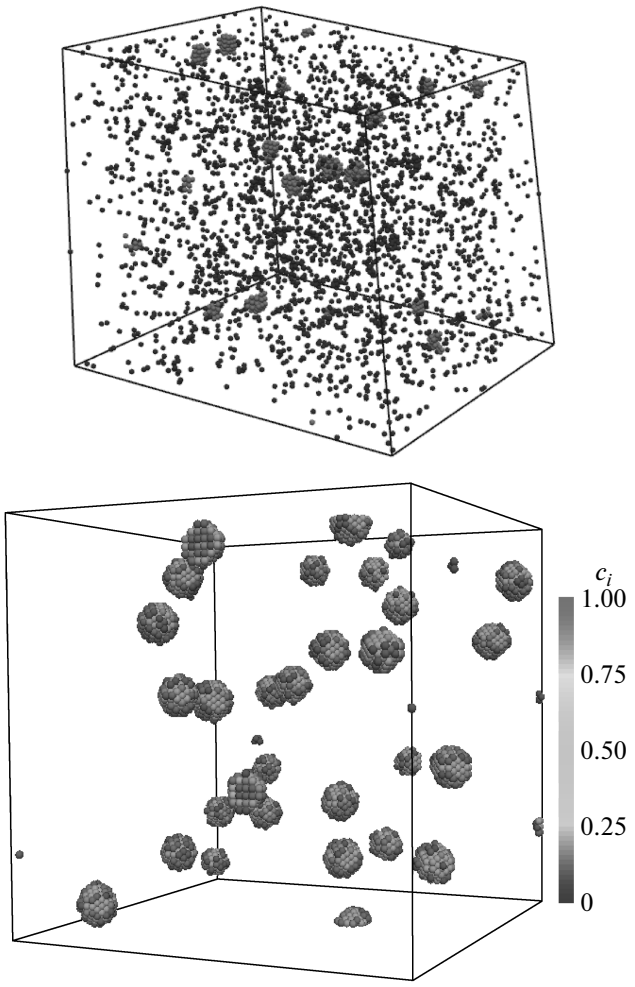

Fig. 17. The same as in Fig. 16, but at the end of nucleation, $t = 1000$ s. Light spheres in the upper frame show copper atoms that belong to some supercritical precipitate (color online [31])

5.2. Features of microstructure at different stages of precipitation

In Figs. 16–19, we show microstructure of the SF-1 alloy state at different stages of the evolution observed in the KMCA and SSA-based simulations. Because the SSA simulation box was twice as large as that used in the KMCA, the total number of precipitates in the SSA-based (lower) frame in each of Figs. 16–19 is about twice that presented in the KMC-based (upper) frame. Figures 16–19 illustrate the processes of nucleation, growth, and coarsening discussed above.

In comparing the KMCA and SSA results in Figs. 16–19, we note that the SSA, as well as any other statistical description, disregards details of particular atomic configurations presented in the KMCA snapshots, but it allows picking out essential features of microstructure that often cannot be easily apprehended in these snapshots. This is illustrated by Fig. 16, where the SSA frame clearly shows a number of regions significantly enriched by copper atoms, that is, precursors of precipitates to be created, while such regions are not clearly seen in the analogous KMC frame. Similar differences in describing precipitates can be seen in Figs. 17–19. The main quantitative characteristics of precipitates, such as their density and sizes discussed above, can be easily determined in both approaches. At the same time, the presence of significant crystalline anisotropy, particularly for not large precipi-

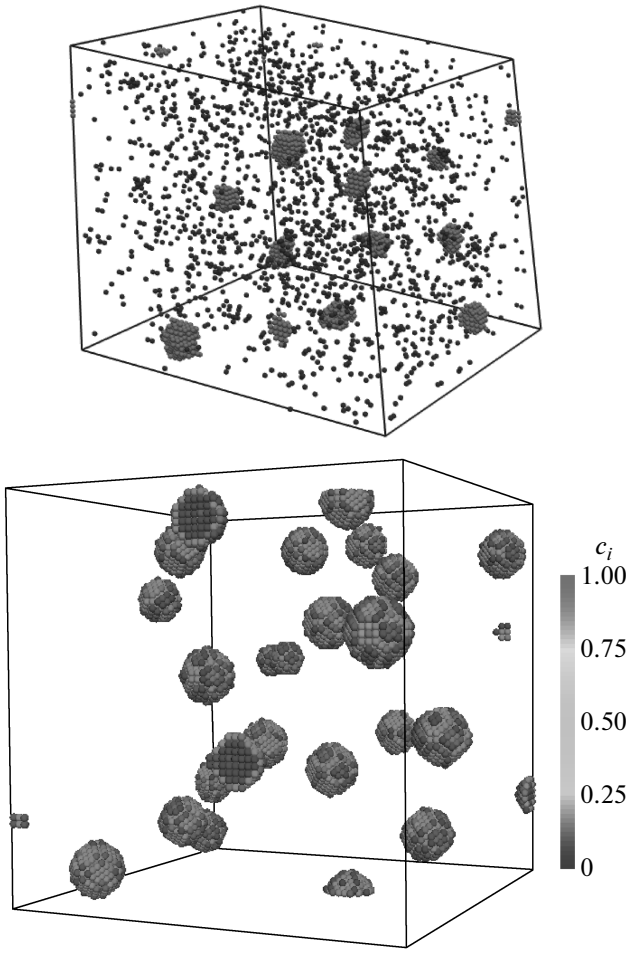

Fig. 18. The same as in Fig. 17, but at the beginning of coarsening, $t = 2000$ s (color online [31])

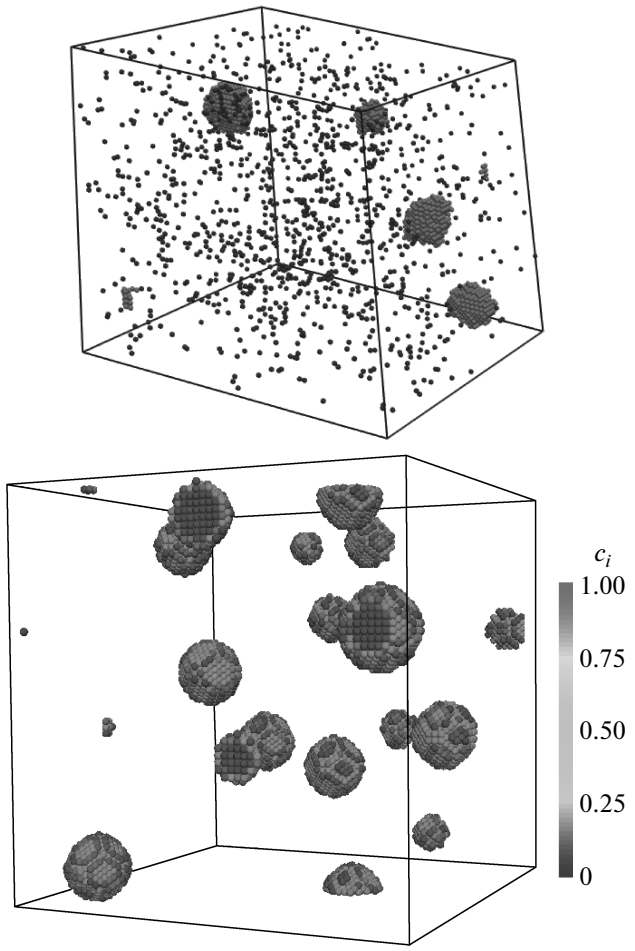

Fig. 19. The same as in Fig. 17, but at some intermediate stage of coarsening, $t = 4000$ s (color online [31])

tates, can be established only after some special analysis in the KMCA [15, 18], but is immediatelly seen in the SSA frames. The difference between two descriptions is also evident for interfaces of precipitates. In the KMCA frames in Figs. 17–19, these interfaces are usually rather sharp but typically not flat and not regular, while in the analogous SSA frames, these interfaces seem to be somewhat diffuse and have typically "intermediate" values of local concentration: $c_i \sim 0.5$. The differences arise because each local concentration c_i in the SSA is obtained by averaging over some locally equilibrated vicinity of site i, that is, over a relatively rapid motion of surface atoms on the "nonfilled" facet considered. At the same time, inner parts of precipitates (for both the KMCA and SSA) include only copper atoms, which is clearly seen in the SSA frames on cuts of precipitates by boundary planes of the simulation box.

Therefore, Figs. 16–19 also illustrate a complementary character of describing the evolution of microstructure by the KMCA and the SSA.

5.3. Kinetics of nucleation

As discussed above, the SSA provides a partly averaged description of atomic distributions, primarily aiming at adequate calculations of locally averaged quantities, such as the density of different precipitates, their structure, morphology, and so on. Therefore, quantitative treatments of phenomena that are mainly determined by fluctuations, such as processes of creation and evolution of under-critical and near-critical embryos, lies outside the scope of the SSA in general. However, as mentioned above, the qualitative changes of microstructure, such as those corresponding to the nucleation process, can often be more easily followed in the

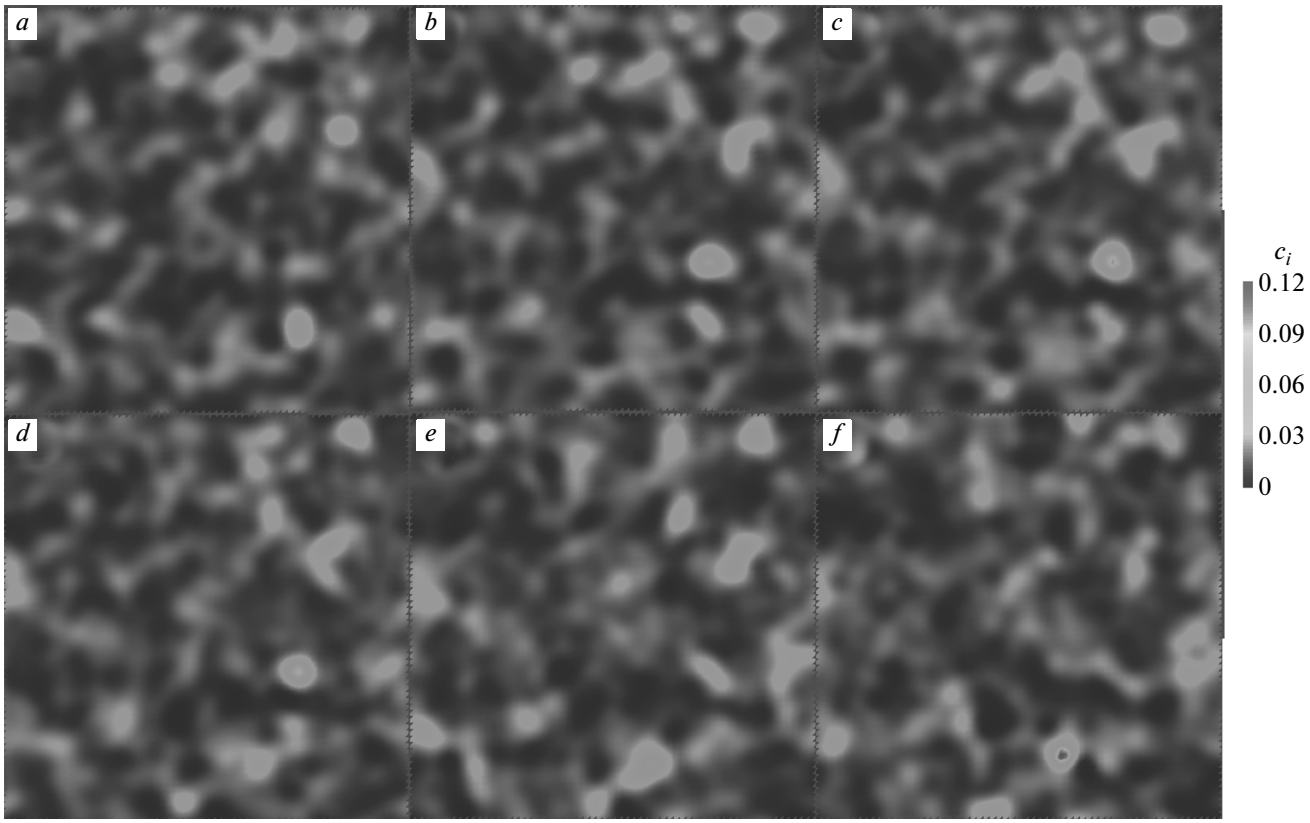

Fig. 20. Distribution of local concentrations within a plane containing several nucleating precipitates for the SF-1 state at the following reduced time t_r values: 7.5 (*a*), 7.9 (*b*), 8.0 (*c*), 8.1 (*d*), 8.5 (*e*), and 9.0 (*f*). For each point $\mathbf{r}$ in the figure, the $c(\mathbf{r})$ value is obtained by interpolation between c_i on the neighboring lattice sites. The relation between coloring and the c_i values is shown in the right part of the figure (color online [31])

SSA rather than in the KMCA. Therefore, it can be instructive to study kinetic details of nucleation with the use of the SSA, even though the scale of fluctuation effects in such a study is most probably underestimated.

Some results of such studies are presented in Figs. 20–22, which illustrate processes of sequent creation of three supercritical embryos for the SF-1 alloy state. Figures 20*a*–*e* also show processes of creation and dissolution of an "undercritical" embryo: the concentration fluctuation in the right central part of these frames first increases to the values $c_i \sim 0.1$, but then decreases and disappears. On the contrary, Figs. 20*d*–*f* illustrate a "successful" nucleation process. The local fluctuation positioned below that discussed in the foregoing first increases in both size and amplitude, and then suddenly shrinks with formation of a "kinetic" supercritical embryo. Later on, this embryo survives and grows, but this growth is first nonmonotonic and includes a "partial dissolution" process illustrated by Figs. 21*a* and 21*b*. We note that at first stages of this process shown in Figs. 20*e* and 20*f*, the embryo is extended and shapeless, while later on, it is rather irregularly shaped, and hence seems to have little in common with the "thermodynamic" critical embryos shown in Fig. 2.

Creation and evolution of two other embryos shown in Figs. 21 and 22 proceed similarly. In both cases, the initial extended and shapeless fluctuation of concentration first suddenly shrinks such that maximum concentrations within it reach "critical" values $c_i \gtrsim 0.12$, after which embryos seem to become "supercritical". Then subsequent fluctuations lead to a partial dissolution of these embryos, but in both cases they survive and start to grow later on. This growth correspond to "sucking" of copper atoms from adjacent regions and thus to depletion of copper concentration in these regions.

The examples considered can also illustrate the kinetic mechanism of nucleation. It can be regarded as a local spinodal decomposition that starts when the amplitudes and extension of a local fluctuative enrichment of concentration become large enough for the

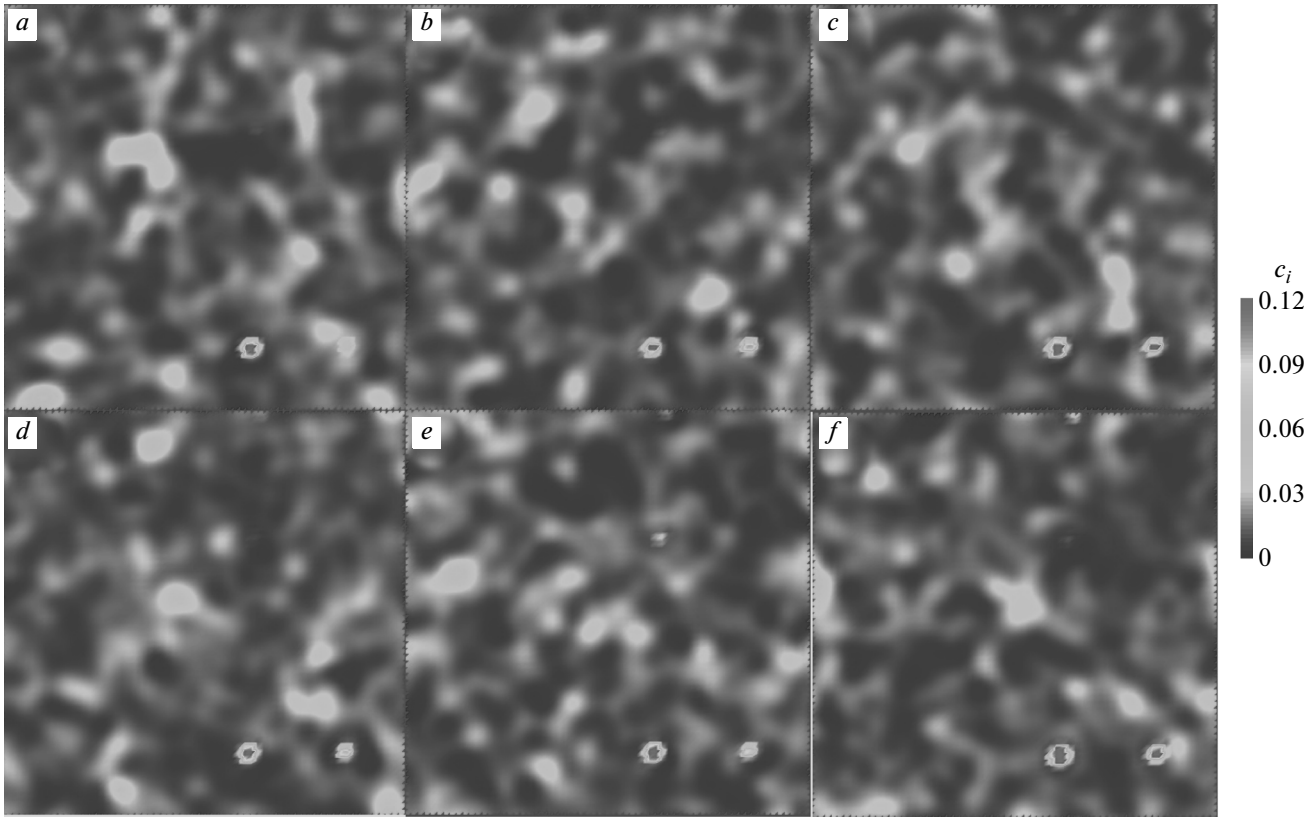

Fig. 21. The same as in Fig. 20, but at the following t_r: 21 (*a*), 24 (*b*), 29 (*c*), 31 (*d*), 34 (*e*), and 38 (*f*) (color online [31])

"uphill diffusion" mechanism characteristic of spinodal decomposition [32] to become operative. In the examples considered, this seems to correspond to local concentrations $c_i \gtrsim 0.07$–0.09 (while the uniform spinodal decomposition boundary, according to Fig. 1, is $c_s \approx 0.045$) in the region $l \gtrsim (7$–$8)a$. Such an interpretation of nucleation as a fluctuation-induced local spinodal decomposition can be useful for a qualitative understanding of many phenomena in this field, in particular, of a large excess in probabilities of nucleation near the binodal curve observed experimentally [36] compared to estimates of the classical theory of nucleation (55).

5.4. Changes in microstructural evolution under variations of temperature or concentration

As mentioned in Sec. 4.1, the kinetic type of alloy decomposition is mainly determined by the value of the reduced supersaturation s in (65), which is less than unity for metastable states under consideration. Low s correspond to the states with the concentration and temperature values (c, T) close to the binodal curve for which a "deep NG" type of evolution with a low density and large sizes of nucleating precipitates is characteristic. An increase in s corresponds to an approach to the spinodal curve and a decrease in nucleation barriers, and hence nucleating precipitates should become smaller (which is illustrated by Table II), while their density should increase. Based on these considerations, we can expect that the reduced supersaturation s is the main parameter determining microstructural evolution, but at a given s, microstructure can also significantly vary with the concentration or temperature.

To illustrate these variations, in Fig. 23 we show microstructure at the end of nucleation for the SF-1, SF-3, and SF-4 alloy states described by Tables 1 and 2 and Fig. 2. In simulations for the SF-4 state (which has the same supersaturation s as the SF-3 state, but higher concentration and temperature), we used $g_0 = 1.9$, the same as for the SF-3 state. Figure 23 shows that in accordance with the foregoing, the increase in the supersaturation s in SF-3 and SF-4 states compared to SF-1 by about 1.5 times leads to a much higher density of nucleated precipitates: by about 3.6 times for the

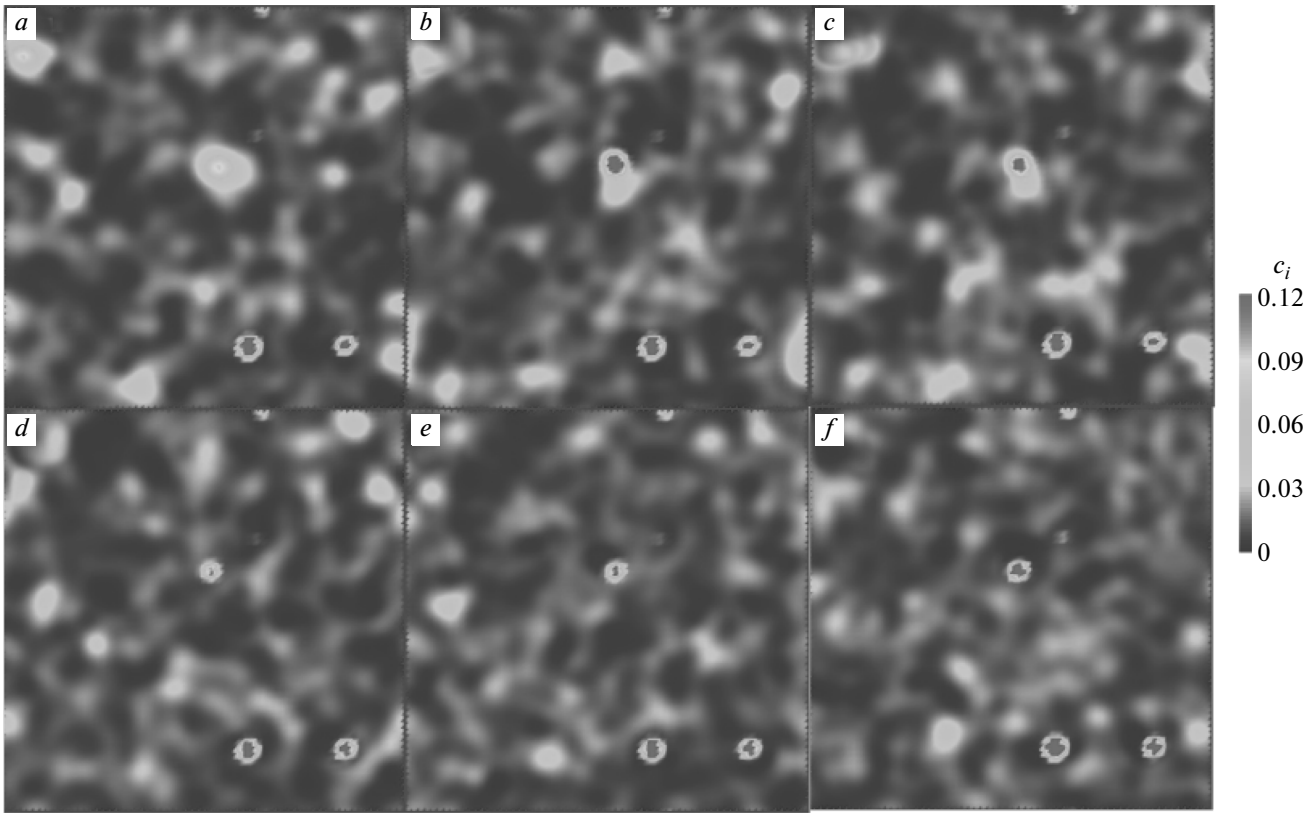

Fig. 22. The same as in Fig. 10, but at the following t_r: 46 (*a*), 47 (*b*), 48 (*c*), 49 (*d*), 50 (*e*), and 53 (*f*) (color online [31])

SF-3 state, and by 2.2 times for the SF-4 state. On the other hand, Figs. 23*b* and 23*c* illustrate differences in microstructure for the same s but different c and T. For the SF-4 state, precipitates are notably larger, while their density is 1.5 times lower than those for the state SF-3. These differences are correlated with differences in characteristics of thermodynamic critical embryos for these two states presented in Table 2 and Fig. 2: both critical sizes and reduced nucleation barrier F_c/T for the SF-4 state notably exceed those for the SF-3 state.

6. CONCLUSIONS

To conclude, we summarize the main results in this work.

1. A consistent and computationally efficient stochastic statistical approach is developed to microscopic studies of the kinetics of decomposition of metastable alloys.

2. In this approach, the description of evolution in terms of a certain reduced time includes no fitting parameters. This reduced time can usually be rescaled to the physical time with the use of several constants, which can be estimated either from comparison to kinetic Monte Carlo simulations or from experiment.

3. For several realistic models of iron–copper alloys studied, the results of this approach typically agree with the kinetic Monte Carlo simulation results within errors of these simulations.

4. Oversimplified model (71) for the important kinetic parameter of the theory, the size of locally equilibrated regions for the nucleation stage, seems to be sufficient for describing the main characteristics of microstructure. But an adequate description of temporal dependences requires using more realistic models discussed in Secs. 4.2 and 5.1.

The authors are much indebted to I. A. Zhuravlev for his help in this work, and to Yu. N. Gornostyrev, P. A. Korzhavy, and G. Martin for the numerous valuable discussions. The work was supported by the Research Technological Center "Ausferr", Magnitogorsk, by the Russian Foundation for Basic Research (grant No. 06-02-16476), by the foundation for Support of Leading Scientific Schools of Russia (grant

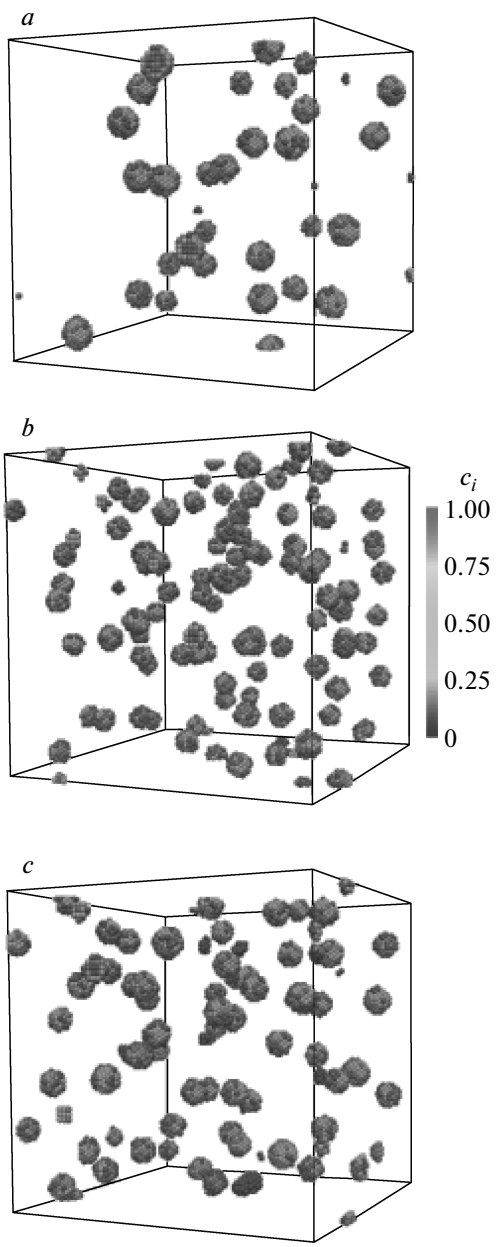

Fig. 23. Distribution of concentrations c_i at the end of nucleation for the following alloy states: SF-1 (a), SF-3 (b), and SF-4 (c) (color online [31])

No. NS-3004.2008.2); and by the program of Scientific Potential Development of Russian Universities (grant No. 2.1.1/4540).

REFERENCES

1. L. D. Landau and E. M. Lifshits, *Statistical Physics*, Nauka, Moscow (1995).
2. E. M. Lifshits and L. P. Pitaevsky, *Physical Kinetics*, Nauka, Moscow (1979).
3. K. Binder, in: *Materials Science and Technology, Vol. 5: Phase Transformations in Materals*, ed. by R. W. Cahn et al., VCH, Weinheim (1991), Chap. 7.
4. F. Soisson and G. Martin, Phys. Rev. B **62**, 203 (2000).
5. M. K. Miller, B. D. Wirth, and G. R. Odette, Mater. Sci. Eng. **353**, 133 (2003).
6. A. Cerezo, S. Hirosawa, G. Sha, and G. D. W. Smitn, in: *Solid→Solid Phase Transformations in Inorganic Materials 2005*, ed. by J. M. Howe et al., TMS, Warrendale (2005), Vol. 1, p. 251.
7. D. Isheim, R. P. Kolli, M. E. Fine, and D. N. Seidman, Scripta Mater. **55**, 35 (2006).
8. R. Rana, W. Bleck, S. B. Singh, and O. N. Mohanti, Mater. Lett. **61**, 2919 (2007).
9. Y. Wang, D. Banerjee, C. C. Su, and A. G. Khachaturyan, Acta Mater. **46**, 2983 (1998).
10. W. Guo, Y. Zong, G. Wang, and Y. Wang, in: *Solid→Solid Phase Transformations in Inorganic Materials 2005*, ed. by J. M. Howe et al. (Ref. [6]), Vol. 2, p. 757.
11. T. Koyama and H. Onodera, Mater. Trans. **46**, 1187 (2005).
12. T. Nagano and M. Enomoto, Scripta Mater. **55**, 223 (2006).
13. C. Zhang and M. Enomoto, Acta Mater. **54**, 4183 (2006).
14. Q. Bronchart, Y. Le Bouar, and A. Finel, Phys. Rev. Lett. **100**, 015702 (2008).
15. F. Soisson, A. Barbu, and G. Martin, Acta Mater. **44**, 3789 (1996).
16. Y. Le Bouar and F. Soisson, Phys. Rev. B **65**, 094103 (2002).
17. E. Clouet, M. Nastar, A. Barbu, C. Sigli, and G. Martin, *Solid→Solid Phase Transformations in Inorganic Materials 2005* (Ref. [6]), Vol. 2, p. 683.
18. F. Soisson and C.-C. Fu, Phys. Rev. B **76**, 214102 (2007).
19. V. Yu. Dobretsov, I. R. Pankratov, A. Yu. Stroev, and V. G. Vaks, *Solid→Solid Phase Transformations in Inorganic Materials 2005* (Ref. [6]), Vol. 1, p. 169.
20. A. Yu. Stroev, I. R. Pankratov, and V. G. Vaks, Phys. Rev. B **77**, 134203 (2008).

21. V. G. Vaks, Phys. Rep. **391**, 157 (2004).

22. K. D. Belashchenko and V. G. Vaks, J. Phys.: Condens. Matter **10**, 1965 (1998).

23. V. G. Vaks and K. Yu. Khromov, Zh. Exp. Teor. Fiz. **133**, 115 (2008) [JETP **106**, 94 (2008)].

24. V. G. Vaks and K. Yu. Khromov, Zh. Exp. Teor. Fiz. **133**, 313 (2008) [JETP **106**, 265 (2008)].

25. V. G. Vaks and G. D. Samolyuk, Zh. Eksp. Teor. Fiz. **115**, 158 (1999) [JETP **88**, 89 (1999)].

26. J. W. Cahn and J. E. Hilliard, J. Chem Phys. **31**, 688 (1959).

27. V. Yu. Dobretsov and V. G. Vaks, J. Phys.: Condens. Matter **10**, 2261 (1998).

28. V. Yu. Dobretsov and V. G. Vaks, J. Phys.: Condens. Matter **10**, 2275 (1998).

29. V. G. Vaks, Pis. Zh. Eksp. Teor. Fiz. **63**, 447 (1996) [JETP Lett. **63**, 471 (1996)].

30. F. Soisson, C. Becquart, N. Castin, C. Domain, L. Malerba, and E. Vincent, J. Nucl. Mater. **406**, 55 (2010).

31. K. Yu. Khromov, F. Soisson, A. Yu. Stroev, and V. G. Vaks, http://arxiv.org/abs/0911.5558.

32. V. G. Vaks, S. V. Beiden, and V. Yu. Dobretsov, Pis. Zh. Eksp. Teor. Fiz. **61**, 65 (1995) [JETP Lett. **61**, 68 (1995)].

33. K. D. Belashchenko, I. R. Pankratov, G. D. Samolyuk, and V. G. Vaks, J. Phys.: Condens. Matter **14**, 565 (2002).

34. P. Glansdorff and I. Prigogine, *Thermodynamic Theory of Structure, Stability and Fluctuations*, Wiley (1971).

35. W. M. Young and E. W. Elcock, Proc. Phys. Soc. Lond. **89**, 735 (1966).

36. T. Miyazaki, T. Kozakai, and C. G. Schoen, *Solid→ Solid Phase Transformations in Inorganic Materials 2005* (Ref. [6]), Vol. 2, p. 271.